

# Diagnosing Forecast Errors in Tropical Cyclone Motion in HWRF

Thomas J. Galarneau, Jr.  
National Center for Atmospheric Research  
Boulder, Colorado

Final Report for the 2013 DTC Visitor Program  
30 April 2014

## Contents of the report:

1. Overview
2. Introduction
3. Data and methods
4. Basin-scale flow errors
5. Case study of TC Katia (2011)
6. Climatology for H213 retrospective
7. Final comments
8. References
9. Figures

## *Corresponding author address:*

Thomas J. Galarneau, Jr.  
National Center for Atmospheric Research  
P.O. Box 3000  
Boulder, CO 80307  
E-mail: tomjr@ucar.edu

## 1. Overview

The aim of this proposal was to utilize a new diagnostic approach developed by Galarneau and Davis (2013) to examine the sources of numerical model forecast error that contribute to degraded tropical cyclone (TC) motion forecasts in the 2013 Hurricane Weather Research and Forecasting (HWRF) model retrospective test. Large errors in the forecast position of a TC (termed the “track error”) are generally preceded (and caused) by errors in the predicted motion of the TC. This new diagnostic approach quantifies errors in predicted TC motion and accounts for errors in the environment wind driven by synoptic-scale weather systems and errors in the vertical depth and radius used to define the steering layer flow. The vertical depth and radius errors are attributed to errors in the structure of the TC vortex and nearby mesoscale flow features.

Application of the TC motion error diagnostic was successfully applied to the 2013 HWRF retrospective test (H213) for the 2010–2012 North Atlantic seasons. Analysis of the H213 forecasts showed that TC motion forecast errors were dominated overall by errors in the environment wind. Errors from the vertical depth and radius were occasionally large, particularly for TCs that were in the process of recurving into midlatitudes. The dominant contributor to environment wind errors for westward and northwestward-moving TCs was subsynoptic-scale errors in the North Atlantic subtropical ridge. For westward-moving TCs, an over-abundance of anticyclonic vorticity in the deep tropics southeast of the TC also contributes to the persistent environment wind error. This vorticity error appears to be associated with reduced convection northeast of South America over the tropical Atlantic. For northeastward-moving TCs, a persistent northeasterly environment wind error contributed to a slow error, and appears to be linked to a midlatitude waveguide that is too zonal.

## 2. Introduction

Despite substantial improvements in tropical cyclone (TC) position (or “track”) forecasts over the last 40 years (Rappaport et al. 2009) that can be attributed to increases in model resolution and available observations (Aberson 2010), and improved data assimilation techniques (Hamill et al. 2011), large forecast errors still occur. The reasons for these large forecast position errors have been extensively documented in the literature, with the overall message being that errors in the environment wind field are the dominant contributor to forecast position errors (e.g., Brennan and Majumdar 2011). These environment wind errors occur frequently in situations where a TC is interacting with flow associated with a midlatitude baroclinic cyclone, or with upper-level outflow associated with other nearby TCs or organized convective systems (e.g., Carr and Elsberry 2000; Kehoe et al. 2007). Tropical cyclone position forecast errors have also been attributed to errors associated with TC intensity and structure (e.g., McTaggart-Cowan et al. 2006), which has implications on the steering flow depth and how the TC interacts with nearby synoptic-scale circulation features. Operational TC track forecasts for TC Sandy (2012) nicely illustrates that despite the substantial improvements in TC track prediction overall, systematic errors do still occur (Fig. 2.1). For forecasts of TC Sandy that were initialized when Sandy was south of Cuba, a distinct right-of-track error was noted as the forecast tracks indicated that Sandy would move out to sea by 26–27 October, rather than hook left toward New Jersey. This error was universal for all of the numerical model forecasts shown from both global and regional models, except for the UKMet. It is these types of errors, especially for TCs that pose a high risk of socioeconomic impact, that motivate continued evaluation of numerical model track forecasts.

Previous studies have suggested that TC motion is driven primarily by the environment wind that comprises flow contributions from synoptic-scale weather systems and near-storm vorticity asymmetries (e.g., Chan and Gray 1982; Holland 1983, 1984; Fiorino and Elsberry 1989; Chan et al. 2002). The environment wind is the residual wind that results from the removal of the TC vortex (e.g., Neumann 1979). Studies have varied on the preferred vertical layer over which the environment wind is averaged to define the steering flow, ranging from the 700–500 hPa layer (e.g., George and Gray 1976) to the tropospheric-deep layer (e.g., Velden and Leslie 1991). In addition to the environment wind in the steering layer, TC motion can also be influenced by the interaction with landmasses (e.g., Holland 1983), sea-surface temperature gradients (e.g., Bender et al. 1993), and the asymmetric distribution of convection in response to vertical wind shear (e.g., Wang and Holland 1996).

The aim of this study is to use the definition of steering flow to determine the factors that contribute to departures in forecasted TC motion in the Hurricane Weather Research and Forecasting (HWRF) model from observations. Specifically, HWRF forecasts from the 2013 retrospective test (H213) will be analyzed and interpreted from a climatological and case study perspective. The period of interest covers the North Atlantic TC seasons from 2010–2012.

### 3. Data and methods

Galarneau and Davis (2013) defined the steering flow as the spatially averaged environment wind that best matches the TC motion. They computed the steering flow by first computing the environment wind every 50 hPa in the 850–200 hPa layer using eight different radii ranging from 1–8° in which to remove the TC vortex. Then for each radius, the pressure-weighted vertically averaged environment wind was computed for layers of increasing depth ranging from 850–800 hPa to 850–200 hPa. For all possible depth and radius combinations, or candidate steering layer values, the magnitude of the vector difference between the actual TC motion and steering flow was computed. The radius and steering layer depth combination that produced the smallest vector residual magnitude was the optimal steering layer definition chosen for the TC at the given time. The optimal steering layer method showed a marked improvement over the deep-layer mean steering method (e.g., Velden and Leslie 1991), by sharpening the agreement between TC motion and steering flow. The close match between TC motion and steering flow allows for quantification of TC motion errors and partition of the difference in steering flow between the forecast and analysis into errors in environment wind, vertical steering depth, and TC removal radius.

Using the steering flow definition defined above, Galarneau and Davis (2013) derived a diagnostic equation that quantitatively assesses the sources for forecast TC motion error. The TC motion error diagnostic equation is defined as

$$\underbrace{\vec{V}_m - \vec{V}_o}_{\text{storm motion error}} = \underbrace{\frac{1}{p_b - p_{to}} \int_{p_{to}}^{p_b} (\hat{\vec{v}}_m - \vec{v}_o) dp}_{\text{environment wind error}} + \underbrace{\frac{1}{p_b - p_{tm}} \int_{p_{tm}}^{p_b} -(\hat{\vec{v}}_m - \vec{v}_m) dp}_{\text{TC removal radius error}} + \underbrace{\frac{1}{p_b - p_{tm}} \left[ \int_{p_{to}}^{p_b} \left( \frac{p_{tm} - p_{to}}{p_b - p_{to}} \right) \hat{\vec{v}}_m dp + \int_{p_{tm}}^{p_{to}} \hat{\vec{v}}_m dp \right]}_{\text{TC steering depth error}} + \text{residual term}$$

where  $p_b=850$  hPa and  $p_t$  is defined as the top of the optimal steering layer,  $\mathbf{V}$  is defined as the TC motion (using positions at time  $\pm 12$  h),  $\mathbf{v}$  is the area-averaged environment wind (TC removed) computed over the optimal radius, and  $\hat{\mathbf{v}}$  is the area-average environment wind (TC removed) computed for the model TC over the radius determined for the observed TC. The subscripts ‘o’ and ‘m’ indicate the observed storm and steering flow and the model storm and steering flow, respectively. The term on the left hand side represents the vector error between the observed and model TC motion. The first term on the right hand side represents the contribution from model environment wind errors in the observed steering flow layer, the second term represents the contribution from differences in the TC removal radius between the model and observed TC in the model steering flow layer, and the third term represents the contribution from differences between the model and observed steering layer vertical depth. The fourth term represents the residual term,

which includes analysis wind errors and storm motion errors introduced by uncertainties in TC position.

The environment wind error term is defined as the model environment wind minus the analysis environment wind integrated over the steering depth for the observed storm, both using the radius defined for the observed storm ( $r_o$ ). Thus, the environment wind error term is a function of only the difference in wind between the analysis and forecast all due to vorticity and divergence differences outside of  $r_o$  since it is this vorticity and divergence that drives the wind inside of  $r_o$ . The next two terms – TC removal radius and vertical steering depth term – arise because we allow the radius and vertical steering depth to differ between the model and observed storm at a given time. In cases when  $p_m=p_{to}$  or when  $\hat{v}_m(p)$  does not vary with pressure (no vertical shear) the steering depth term will go to zero. Likewise, when  $r_m=r_o$  the radius term will go to zero. Because the TC motion error diagnostic equation uses a local coordinate system, Galarneau and Davis (2013) analyzed 24-h TC position forecasts so that the spatial variation of the environment wind between the observed and forecast TC locations could be ignored. It is likely, however, that notable 24-h forecast TC motion errors will contribute to large position errors at longer lead times. However, there is no formal limitation to applying this diagnostic to any lead-time.

This study will apply the motion error diagnostic to 24-h forecasts of TC motion from the gridded H213 dataset. The forecasted motion is computed using the “ATCF” output, and the steering flow using gridded winds on pressure levels from the outer domain (~27 km grid spacing). The forecasts are compared to the motion of the observed TC as determined from the Hurricane Best Track Database (HURDAT). The steering flow for the observed storms is computed using the NCEP Global Forecast System (GFS) analyses at a horizontal resolution of  $0.5^\circ$ . The H213 data is interpolated to a regular latitude-longitude grid at  $0.5^\circ$  grid spacing in order to match the resolution and grid structure of the GFS analyses. The coverage of the H213 outer domain is shown in Fig. 3.1. The 850 hPa meridional wind speed shows the position of TCs Katia and Lee in the 24-h H213 forecast verifying at 0000 UTC 5 September 2011 (Fig. 3.1a). The details on how the TC vortex is removed for the steering layer flow calculation follows Galarneau and Davis (2013). An example of the wind field after vortex removal is shown in Fig. 3.1b.

#### **4. Basin-Scale flow errors**

The track forecast statistics for the available operational models and the H213 retrospective test are shown in Fig. 4.1a. The H213 track forecasts are significantly improved over all other models except for the GFS and GFS ensemble. Most noteworthy is the significant improvement in H213 relative to the operational HWRF at all forecast lead times. The forecast track bias for the global models is generally westward in the GFS and Canadian model (CMC) deterministic and ensemble runs (Fig. 4.1b). The error shifts to eastward after 96 hours for the GFS, and north-northwestward for the CMC models. For the regional model forecasts, a distinct northeastward track error develops after 72 hours, and is indicative of the persistent right-of-track error, or early recurvature error

(Fig. 4.1c). The H213 bias, however, shows a remarkable reduction in the so-called early recurvature problem compared to the operational HWRF. Overall, the H213 track forecasts characteristics behave very similarly to the deterministic GFS.

As a first step in diagnosing the 24-h track forecast errors in H213, the synoptic-scale flow errors for 2010–2012 are examined. The outer domain in H213 is placed over varying geographical regions depending on the location of the TC of interest. Since the outer domain position is not static, examining basin wide synoptic conditions is problematic. Figure 4.2 shows the frequency of occurrence for the outer domain position for the retrospective period. Note that the outer nest almost always covers the western North Atlantic, with a frequency over 95%. The frequency linearly decreases zonally, reaching 35% near West Africa and Baja California. Since the domain covers most of the North Atlantic basin nearly 50% of the time, one can generate composite mean maps comprised of data from the outer domain and missing values from regions outside the domain.

Figure 4.3 shows the composite mean 200 hPa geopotential height and wind from the 2013 retrospective test period for the GFS analysis and 24-h H213 forecasts. The most robust differences are located over the tropical eastern North Pacific and eastern North Atlantic. A stronger meridional component to the upper-level flow is apparent over the eastern North Pacific in the GFS analysis compared to the H213 forecasts, and suggests that tropical convection is a bit underdone in the 24-h H213 forecast. The northeasterly flow at 200 hPa in the GFS analysis is representative of the meridional overturning circulation that is enhanced by convection in the upward branch near 10–15°N latitude. Minor differences are apparent in midlatitudes, with the westerly jet axis displaced slightly farther north in the 24-h H213 forecasts compared to the GFS analysis. The zonal wind error field highlights this error by showing a weak westerly wind error over the North Atlantic in the 30–40°N latitude band (Fig. 4.4a). Note that the easterly winds are too strong in the tropics in H213, and is likely linked to the difference in meridional component shown in Fig. 4.3.

Synoptic-scale flow differences at 700 hPa are evident in the same regions as 200 hPa (Fig. 4.5). Note the most prominent wind differences are located in the tropical eastern North Pacific and Atlantic (see also Fig. 4.4b). The tropical easterlies are too weak over much of the central tropical North Atlantic, and the subtropical ridge is a broader structure with the easterly (westerly) flow to its south (north) displaced farther equatorward (poleward) compared to the GFS analysis. Although there appear to be distinct signatures in the synoptic-scale flow errors over the North Atlantic, these errors must be examined in the TC-relative framework in order to assess the relative importance of these errors in driving errors in the forecasted TC motion.

## **5. Case study of TC Katia (2011)**

This section provides a case study of TC Katia (2011) to show an illustrative example of how the TC motion error diagnostic equation works, and how to interpret errors associated with the individual terms in the equation. TC Katia was a long-lived TC

that originated as an African easterly wave over the eastern North Atlantic on 28 August 2011 (Fig. 5.1). Katia occurred during a relatively active period of TCs over the North Atlantic. Katia moved west-northwestward over the tropical North Atlantic while interacting with a series of subsynoptic-scale upper-level troughs over the west-central North Atlantic (see also Fig. 5.2). Specifically, interaction with upper-level features occurred on 2–4 and 7–8 September (Figs. 5.2b–d,g–h). Enhanced northerly deep-layer vertical wind shear during the passage of the upper-level troughs contributed to an asymmetric distribution of convection (Fig. 5.1). The H213 track forecasts for Katia are characterized by small along-track errors and nearly negligible across track errors (Fig. 5.1), indicating that the speed of motion was the primary forecast problem as Katia approached the point of recurvature.

The TC motion error diagnostic terms for 24-h H213 forecasts verifying at 0000 UTC 3–10 September is shown in Fig. 5.3. The diagnostic terms are highly variable during the period likely due to the rapidly evolving synoptic-scale flow that accompanied the subsynoptic-scale upper-level trough passages. Partial cancellation between the motion error diagnostic terms contributed to small motion errors overall that were generally southward during trough interactions and northward otherwise, prior to recurvature. The residual term is relatively small for all of the forecasts.

The TC motion error diagnostic for the 24-h H213 forecast verifying at 0000 UTC 5 September 2011 shows that the small northward motion error results from partial cancellation between a northward environment wind error, and south-southwestward vertical depth error (Fig. 5.3). Figure 5.4a shows the environment wind error term, and illustrates how Katia is embedded in a southerly environment wind error approaching  $1.5 \text{ m s}^{-1}$  that is driven by an anticyclonic circulation error on the east side and a cyclonic circulation error on the west side of Katia. The former is associated with the absence of a lobe of cyclonic vorticity that extends southeastward from Katia in the H213 forecast compared to the analysis (Figs. 5.4b,c). The latter is associated with reduced anticyclonic vorticity west of Katia in the H213 forecast compared to the analysis. The environment wind error for Katia was driven by near-storm subsynoptic-scale differences in the vorticity structure. For cases like this, it is hypothesized that near-storm dropsonde observations may have a relatively large impact on the analysis and subsequent forecast.

A south-southwestward vertical depth error over  $1.0 \text{ m s}^{-1}$  partially cancels the northward environment wind error (Fig. 5.3). The vertical depth term arises because the steering layer depth for the forecasted storm (850–350 hPa layer) is shallower than for the observed storm (850–200 hPa layer), and hence, the broad upper-level southwesterly flow ahead of the upper-level trough to the northwest does not impact the forecasted storm motion (Fig. 5.5). The shallower steering layer depth in the H213 forecast compared to the analysis is consistent with the intensity error. The intensity of the storm in the H213 forecast was 74 knots/975 hPa, while for the observed storm was 90 knots/957 hPa.

An illustrative example of a TC removal radius error is shown in Fig. 5.6 for the H213 24-h forecast verifying at 0000 UTC 7 September 2011. For this verifying time, a

west-northwestward motion error near  $0.7 \text{ m s}^{-1}$  is balanced by a northwestward environment wind error of  $\sim 0.3 \text{ m s}^{-1}$  and a southwestward radius error of  $\sim 0.5 \text{ m s}^{-1}$  (Fig. 5.3). The southwestward radius error is driven by near-storm vorticity asymmetries, specifically a region of anticyclonic vorticity just west of Katia in the H213 forecast (Figs. 5.6a,b). This anticyclonic vorticity “bulls-eye” is absent in the analysis (Fig. 5.6c). It appears that the TC removal radius is smaller for the forecasted storm ( $3^\circ$ ) compared to the observed storm ( $4^\circ$ ) because the anticyclonic vorticity feature is important in steering the forecasted TC. This feature is not present in the analysis, and hence, is not a contributor to the steering of the observed TC.

In summary, the motion forecasts for TC Katia (2011) were highly variable throughout its life cycle. More importantly, departures in the forecasted motion from the observed motion were driven by seemingly small differences in the structure of nearby subsynoptic-scale vorticity features associated with the TC itself and the ridge ahead of the synoptic-scale trough to the northwest. Proper representation of these subsynoptic-scale features in the model initial fields, as well as proper evolution of these features in the subsequent forecasts, are key for more accurate prediction of TC motion in short-range forecasts. The next section will examine the motion errors from a climatological perspective and attempt to determine whether more systematic biases exist in the short-range H213 model forecasts.

## 6. Climatology for H213 retrospective period

The aim of this section is to examine the TC motion errors for 24-h H213 forecasts during the 2013 retrospective period 2010–2012. We examine TC motion errors from a climatological perspective here in order to assess whether any systematic biases in TC motion exist, and if so, identify the source of these errors. Figure 6.1 shows the geographical distribution of 24-h H213 forecasts for the retrospective period. The TC locations are coded by the direction of motion of the observed TC, and are defined as westward- (bearing of  $240\text{--}300^\circ$ ), northwestward- (bearing of  $300\text{--}360^\circ$ ), and northeastward-moving (bearing of  $0\text{--}60^\circ$ ) TCs. The TCs were stratified by motion under the assumption that TCs in different synoptic-scale background flows may exhibit different motion biases in the H213 forecasts.

### *a. westward-moving TCs*

In comparing the definition of optimal steering layer flow for forecasted and observed TCs, the 24-h H213 forecasts for westward-moving TCs are characterized by a relatively larger frequency of smaller TC removal radii and deeper steering layer depths compared to the GFS analysis (Fig. 6.2a,b). The tendency for TCs in H213 to be steered by a deeper layer flow may be related to the bogus vortex used for initialization. While aspects of vortex structure could be examined in detail in a more comprehensive study, the differences in steering layer depth and radius suggests that the H213 TCs are steered by a different steering layer flow compared to observed TCs early in the forecast. The distribution of the vector magnitude for the individual terms of the TC motion error diagnostic is shown in Fig. 6.3. The actual motion, environment wind, and TC removal

radius errors are significantly larger than the residual term during 2010–2012 (Fig. 6.3a). Scatterplots for the individual terms are shown in Fig. 6.4. Note that both the actual motion and environment wind error indicate a  $\sim 0.5$  m/s northeastward motion error for all westward-moving TCs (Fig. 6.4a,b). The northeastward motion error is better defined for westward-moving TCs located within the main development region (MDR) as indicated on Fig. 6.1. Scatterplots for the residual and radius terms do not show any persistent directional error, while the depth term hints at a northeastward-directed error (Figs. 6.4c–e).

The mean vertical profile of environment wind is shown in Fig. 6.5a. Note that the environment wind for 24-h H213 forecasts shows a southwesterly error below 700 hPa and a southeasterly error above 450 hPa. The environment wind differences between the GFS analysis and 24-h H213 forecasts in the upper troposphere are not significant due to the increased variance. The wind error in the lower troposphere, however, indicates that the southwesterly wind error is more robust. The composite mean environment wind error at 850 hPa shows that the southwesterly error occurs in conjunction with a cyclonic wind error west of the TC and an anticyclonic wind error southeast of the TC (Fig. 6.5b). The cyclonic-anticyclonic wind error couplet appears to be associated with reduced anticyclonic vorticity west of the TC and increased anticyclonic vorticity southeast of the TC (Fig. 6.6). The former is associated with errors in the western extent of the subtropical ridge.

#### *b. northwestward-moving TCs*

For northwestward-moving TCs over the western North Atlantic (Fig. 6.1), there is a relatively higher frequency of small TC removal radii compared to the GFS analysis (Fig. 6.2c). Minor differences are apparent for the steering layer depth (Fig. 6.2d). All of the terms in the TC motion error diagnostic equation are significantly larger than the residual term for the retrospective period (Fig. 6.3b). Scatterplots for the individual diagnostic terms show that northwestward-moving TCs are characterized by an average west-northwestward motion error (Fig. 6.7a) that is comprised of a westward environment wind error near 0.5 m/s (Fig. 6.7b), a weak southeastward TC removal radius error (Fig. 6.7d) and a northward steering layer depth error near 0.4 m/s (Fig. 6.7e). The residual error is comparatively small (Fig. 6.7c). Effects from the individual diagnostic terms result in a TC motion that is too fast and left-of-track in the 24-h H213 forecasts (error characteristics that are similar to the Katia case study shown earlier), which can be a particularly problematic forecast issue since these storms are in the process of recurving near the eastern U.S. coastline (Fig. 6.1).

The composite mean environment wind profile shows that flow is too southeasterly in the 24-h H213 forecasts compared to the GFS analysis (Fig. 6.8a). The error is most robust in the 600–400 hPa layer, which is shown in Fig. 6.8b. The enhanced southeasterly flow in the 24-h H213 forecasts appears to be associated with an anticyclonic wind error that extends from northeast of the TC to northwest of the TC. The anticyclonic wind errors are associated with errors in the western extent of the subtropical

ridge and the structure of the ridge ahead of the midlatitude trough approaching from the west (Fig. 6.9).

### *c. northeastward-moving TCs*

For northeastward-moving TCs over the western North Atlantic (Fig. 6.1) there are minor differences in the steering layer definition (Fig. 6.2e,f), with the actual, environment wind, and steering layer depth terms significantly larger than the residual on average for 2010–2012 (Fig. 6.3c). A distinct southwestward TC motion error is apparent for the H213 retrospective, which is interpreted as TCs that move too slow in the 24-h H213 forecasts (Fig. 6.10a). The southwestward TC motion error is attributed to a northeasterly environment wind error  $> 1.0$  m/s, equivalent to error growth near 100 km/day (Fig. 6.10b). The northeasterly environment wind error (see also Fig. 6.11a) appears to be associated with an anticyclonic error to the northwest and a cyclonic error to the southeast of the forecasted TC (Fig. 6.11b). This synoptic-scale error pattern is indicative of a trough to the northwest and ridge to the southeast that are both too weak, resulting in an environment steering flow and midlatitude waveguide that is too zonal (Fig. 6.12). This result is also apparent in the NCEP GFS forecasts, which are characterized by midlatitude flow that is increasingly zonal at longer lead times (not shown). It is hypothesized that errors in the synoptic-scale flow in the GFS forecasts may be influencing the synoptic-scale flow in HWRF, which impacts TC motion and track forecasts particularly for TCs in the subtropics and midlatitudes.

## **7. Final remarks**

Galarneau and Davis (2013) introduced a new diagnostic method for quantifying the phenomena responsible for errors in TC storm track. The method is founded on the notion that errors in storm motion at relatively short lead times (12–48 h) lead to large position errors at later times. The method incorporates aspects of storm structure, such as the depth of the vortex and near-field asymmetries, as part of a comprehensive analysis that formally separates errors in environmental synoptic-scale wind from errors in storm structure, and quantifies how these errors contribute to storm motion errors in numerical weather prediction model forecasts. The value of this new diagnostic approach is that it can be applied to TC motion forecasts from any numerical modeling system. The aim of this DTC Visitor Program research proposal was to apply the TC motion error diagnostic to 24-h TC motion forecasts from the H213 retrospective test covering selected storms from 2010 and all storms from the 2011 and 2012 North Atlantic TC season. Vorticity inversion was used to quantify the importance of specific synoptic-scale weather systems that contribute to forecast errors in the environment TC steering flow, which helped aid the interpretation of the results from the TC motion error diagnostic.

While analysis of a subset of 24-h TC motion forecasts from H213 revealed that the short-range slow and right-of-track bias was greatly reduced compared to the operational HWRF forecasts, systematic steering flow errors still exist for TCs moving westward, northwestward, and northeastward. For westward-moving TCs, an average northeastward motion error was linked to errors in the structure of the North Atlantic subtropical ridge. It appears that the subtropical ridge does not extend far enough west in

the 24-h H213 forecast. The attendant cyclonic wind error northwest of the TC contributes to the northeastward motion error. For northwestward-moving TCs, vorticity asymmetries near the TC vortex are particularly important. These TCs were dominated by a northwestward motion error – too fast and left-of-track – that was driven by errors in the western extent of the subtropical ridge northeast of the TC and errors in the ridge ahead of the approaching midlatitude trough northwest of the TC. An example of the climatological errors for northwestward-moving TCs is shown in the TC Katia case study, which additionally highlights the importance of flow associated with subsynoptic-scale weather systems in the motion of TCs. For northeastward-moving TCs, a distinct southwestward TC motion error was apparent, which was interpreted as TCs that move too slow in the H213 forecasts. The northeasterly environment wind error appears to be associated with an anticyclonic error to the northwest and a cyclonic error to the southeast of the forecasted TC. This synoptic-scale error pattern is indicative of a trough to the northwest and ridge to the southeast that are both too weak, resulting in an environment steering flow and midlatitude waveguide that is too zonal. Although not documented in this report, the zonal midlatitude waveguide/jet is also apparent in the NCEP GFS forecasts, which are characterized by midlatitude flow that is increasingly zonal at longer lead times. It is hypothesized that errors in the synoptic-scale flow in the GFS forecasts may be influencing the synoptic-scale flow in HWRF, which impacts TC motion and track forecasts particularly for TCs in the subtropics and midlatitudes.

Following the diagnosis of TC motion forecasts from H213 documented herein, it is recommended that this work is extended to both the next HWRF retrospective test (H214) and the version of the NCEP Global Forecast System (GFS) used as initial and boundary conditions for H214. This approach will allow assessment of the differences in TC motion errors between H213, H214, and GFS, and will begin to address the following questions:

- What are the dominant drivers of motion (and track) errors in H214?
- What factors are contributing to the improvements in track forecasts in H214 compared to H213<sup>1</sup>? Is it entirely due to a reduction in errors in the environment wind (and nearby synoptic-scale weather system) or also related to improvements in storm structure (manifested as steering layer depth and horizontal scale)?
- In comparing H214 and GFS TC motion forecasts, what is the added value of H214 over the "parent" GFS? What factors lead to departures in TC motion forecasts between H214 and GFS?

In addition to the science questions listed above, any persistent TC motion errors can be linked to the behavior of model physical processes (i.e., physics packages).

---

<sup>1</sup> Improvements in track forecasts in H214 compared to H213 have been noted (V. Tallapragada 2014, personal communication).

## 8. References

- Aberson, S. D., 2010: 10 years of hurricane synoptic surveillance (1997–2006). *Mon. Wea. Rev.*, **138**, 1536–1549.
- Bender, M. A., I. Ginis, and Y. Kurihara, 1993: Numerical simulation of tropical cyclone–ocean interaction with a high-resolution coupled model. *J. Geophys. Res.*, **98**, 23245–23263.
- Brennan, M. J., and S. J. Majumdar, 2011: An Examination of Model Track Forecast Errors for Hurricane Ike (2008) in the Gulf of Mexico. *Wea. Forecasting*, **26**, 848–867.
- Carr, L. E., and R. L. Elsberry, 2000: Dynamical Tropical Cyclone Track Forecast Errors. Part I: Tropical Region Error Sources. *Wea. Forecasting*, **15**, 641–661.
- Chan, J. C. L., and W. M. Gray, 1982: Tropical Cyclone Movement and Surrounding Flow Relationships. *Mon. Wea. Rev.*, **110**, 1354–1374.
- Chan, J. C. L., F. M. F. Ko, and Y. M. Lei, 2002: Relationship between Potential Vorticity Tendency and Tropical Cyclone Motion. *J. Atmos. Sci.*, **59**, 1317–1336.
- Fiorino, M., and R. L. Elsberry, 1989: Some aspects of vortex structure related to tropical cyclone motion. *J. Atmos. Sci.*, **46**, 975–990.
- Galarneau, T. J., Jr., and C. A. Davis, 2013: Diagnosing forecast errors in tropical cyclone motion. *Mon. Wea. Rev.*, **141**, 405–430.
- George, J. E., and W. M. Gray, 1976: Tropical Cyclone Motion and Surrounding Parameter Relationships. *J. Appl. Meteor.*, **15**, 1252–1264.
- Hamill, T. M., J. S. Whitaker, D. T. Kleist, M. Fiorino, and S. G. Benjamin, 2011: Predictions of 2010's Tropical Cyclones Using the GFS and Ensemble-Based Data Assimilation Methods. *Mon. Wea. Rev.*, **139**, 3243–3247.
- Holland, G. J., 1983: Tropical Cyclone Motion: Environmental Interaction Plus a Beta Effect. *J. Atmos. Sci.*, **40**, 328–342.
- Holland, G. J., 1984: Tropical Cyclone Motion. A Comparison of Theory and Observation. *J. Atmos. Sci.*, **41**, 68–75.
- Kehoe, R. M., M. A. Boothe, and R. L. Elsberry, 2007: Dynamical Tropical Cyclone 96- and 120-h Track Forecast Errors in the Western North Pacific. *Wea. Forecasting*, **22**, 520–538.
- McTaggart-Cowan, R., L. F. Bosart, J. R. Gyakum, and E. H. Atallah, 2006: Hurricane Juan (2003). Part II: Forecasting and Numerical Simulation. *Mon. Wea. Rev.*, **134**, 1748–1771.
- Neumann, C. J., 1979: On the use of deep-layer-mean geopotential height fields in statistical prediction of tropical cyclone motion. Preprints, *6th Conference on Probability and Statistics in Atmospheric Sciences*, Boston, MA, Amer. Meteor. Soc., 32–38.
- Rappaport, E. N., 2009: Advances and challenges at the National Hurricane Center. *Wea. Forecasting*, **24**, 395–419.
- Velden, C. S., and L. M. Leslie, 1991: The Basic Relationship between Tropical Cyclone Intensity and the Depth of the Environmental Steering Layer in the Australian Region. *Wea. Forecasting*, **6**, 244–253.
- Wang, Y., and G. J. Holland, 1996: Tropical Cyclone Motion and Evolution in Vertical Shear. *J. Atmos. Sci.*, **53**, 3313–3332.

## 9. Figures

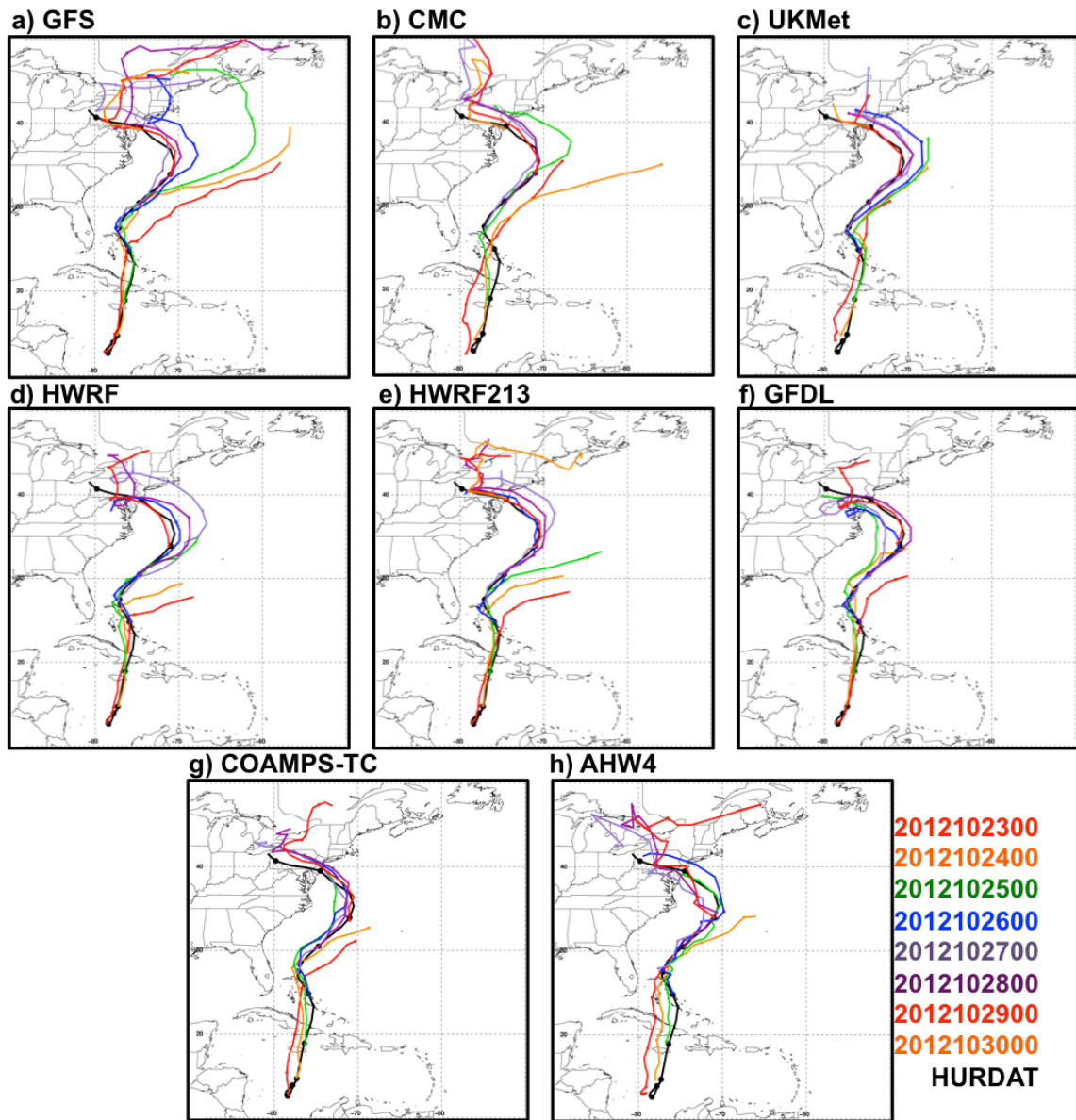
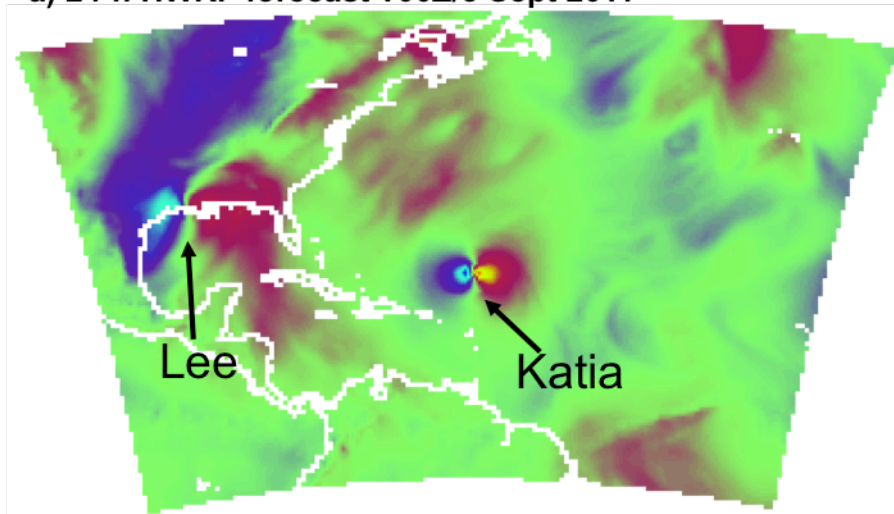


Figure 2.1: HURDAT (black lines) and model (colored lines) track forecasts of TC Sandy (2012) initialized at 0000 UTC 23–30 October from the (a) GFS, (b) CMC, (c) UKMet, (d) operational HWRf, (e) H213 retrospective test, (f) GFDL, (g) COAMPS-TC, and (h) NCAR AHW numerical models. The track forecasts are color coded by the key on the lower right, and the 0000 UTC positions are marked by filled circles.

a) 24-h HWRf forecast v00Z/5 Sept 2011



b) 24-h HWRf forecast v00Z/5 Sept 2011 (Katia removed)

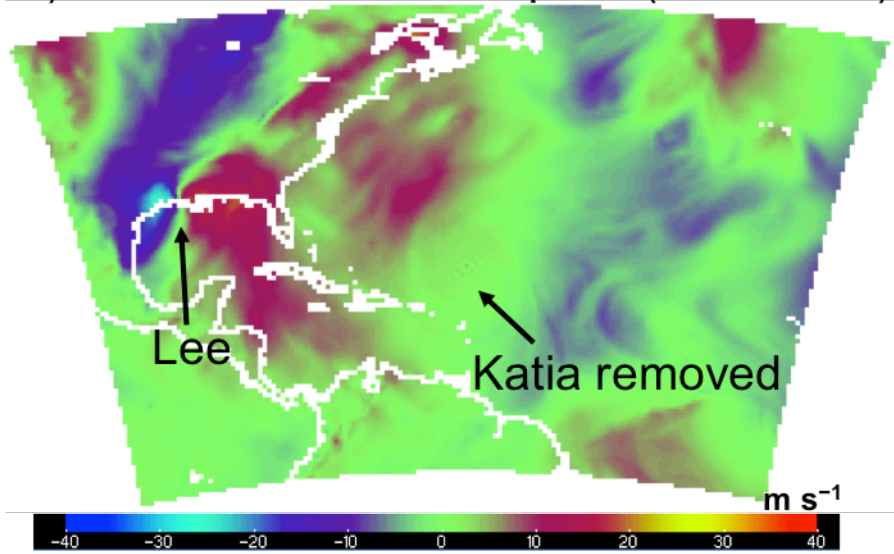
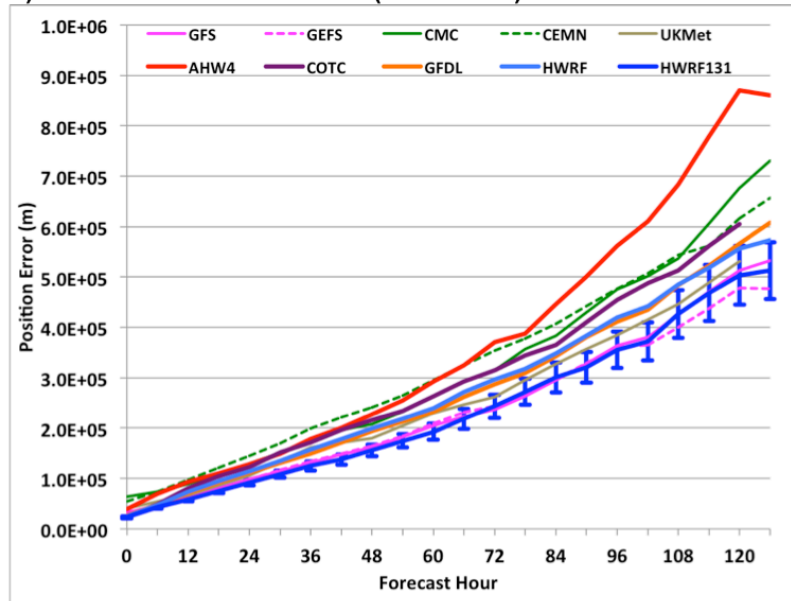
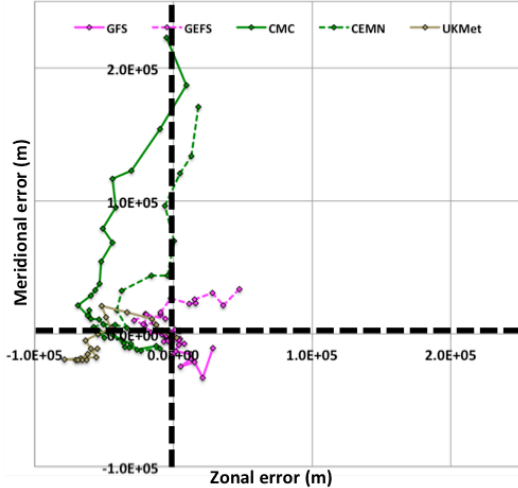


Figure 3.1: (a) 24-h H213 forecast of 850-hPa meridional wind component verifying at 0000 UTC 5 September 2011. (b) As in (a), except with TC Katia removed using vorticity inversion.

a) Mean absolute track error (2010–2012)



b) Global model track bias (2010–2012)



c) Regional model track bias (2010–2012)

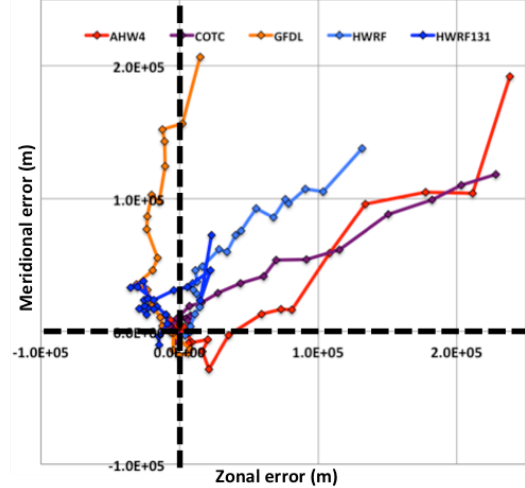


Figure 4.1: (a) Mean absolute track error, (b) global model track bias, and (c) regional model track bias for the H213 retrospective test period of 2010–2012. Individual numerical models are color coded by the key in each panel.

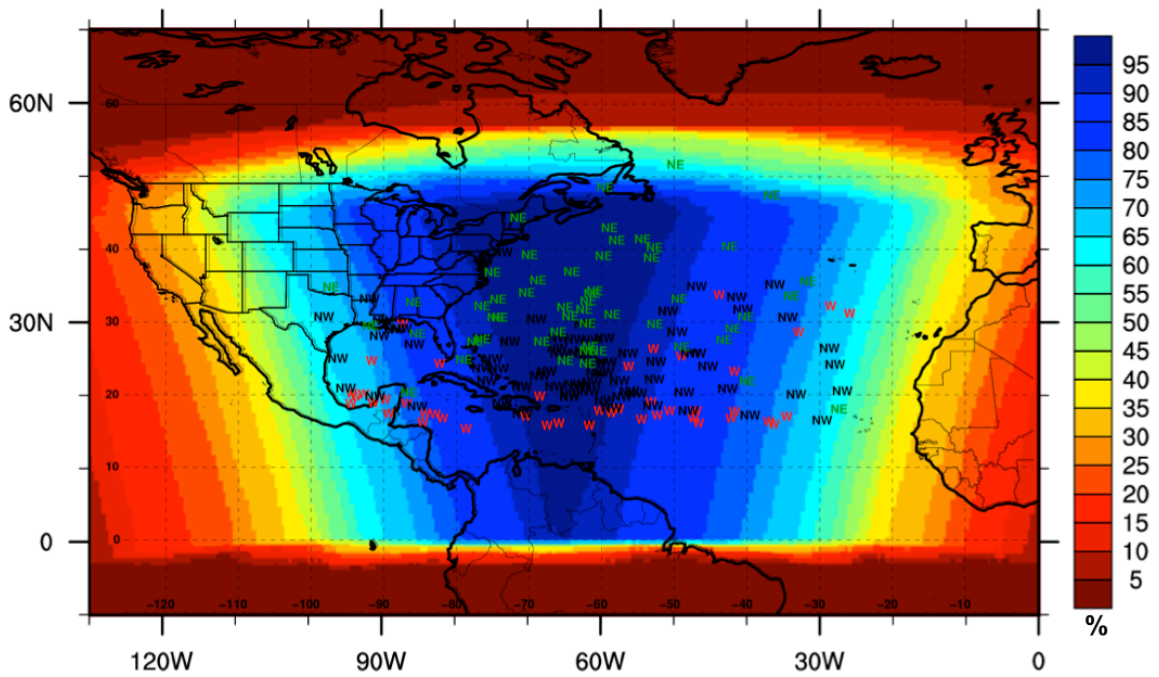


Figure 4.2: Frequency (shaded according to the color bar in %) of the location of the H213 27-km outer domain during the retrospective test. TC locations in the 24-h H213 forecasts are shown, stratified by TC motion as westward- (W), northwestward- (NW), and northeastward-moving (NE).

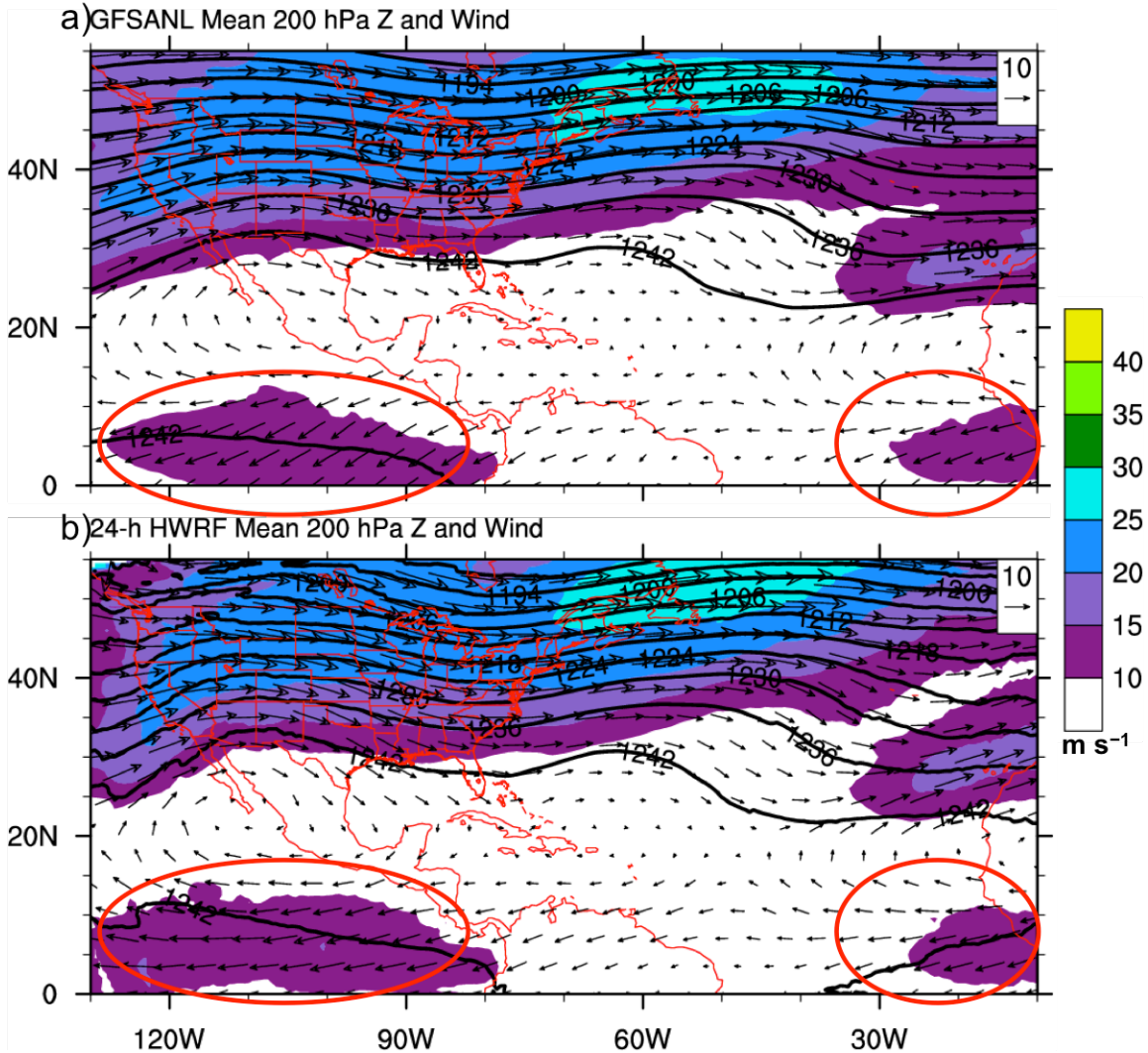


Figure 4.3: Mean 200 hPa geopotential height (contours in dam) and wind (vectors with magnitude shaded according to the color bar in  $\text{m s}^{-1}$ ) for the (a) GFS analysis and (b) 24-h H213 forecasts during the 2013 retrospective test period (2010–2012). The red circles mark error regions in the tropics.

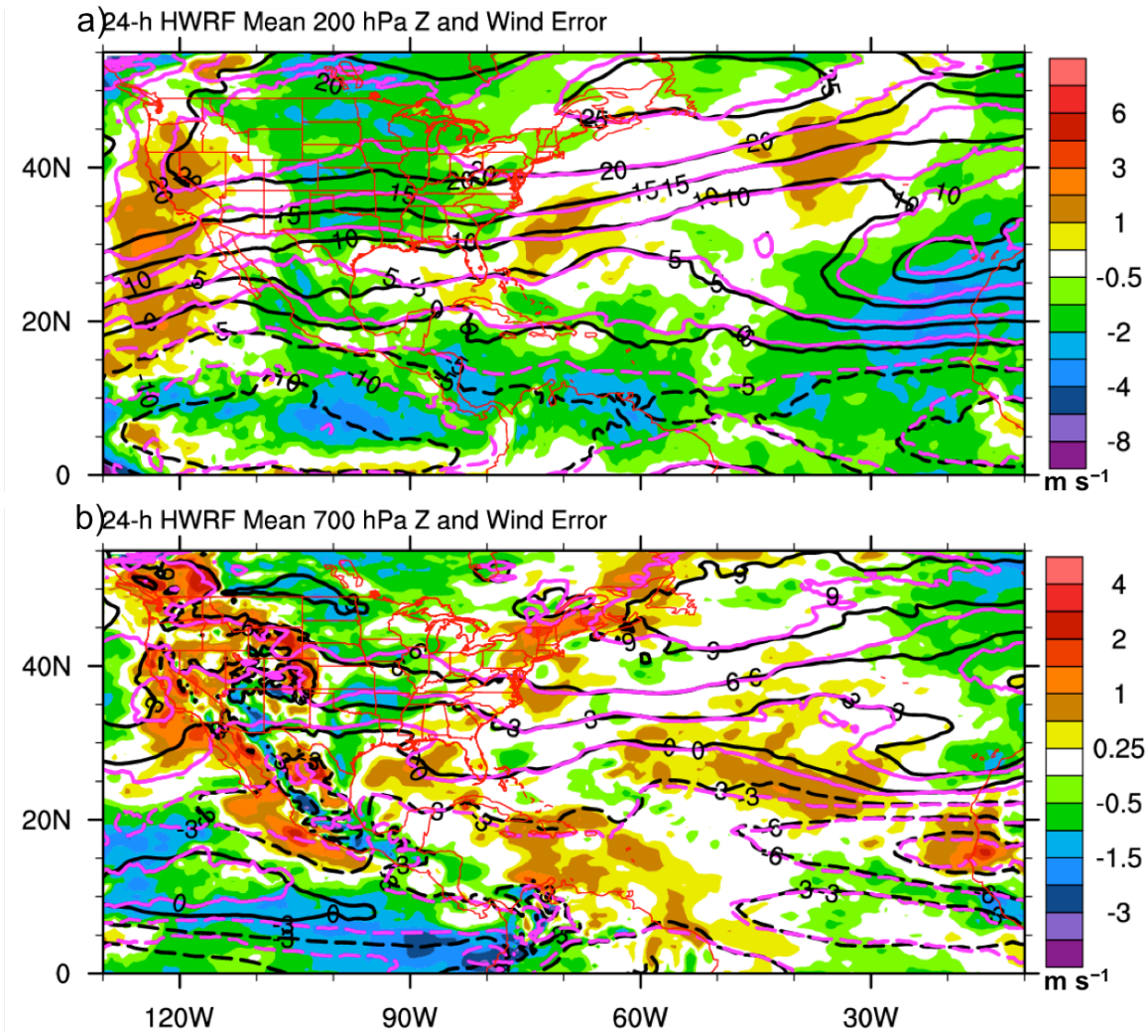


Figure 4.4: Mean 24-h zonal wind error (H213 minus GFS; shaded according to the color bar in m/s) and zonal wind (contours in m/s; GFS analysis in black; 24-h H213 forecasts in magenta) at (a) 200 and (b) 700 hPa during the 2013 retrospective test period (2010–2012).

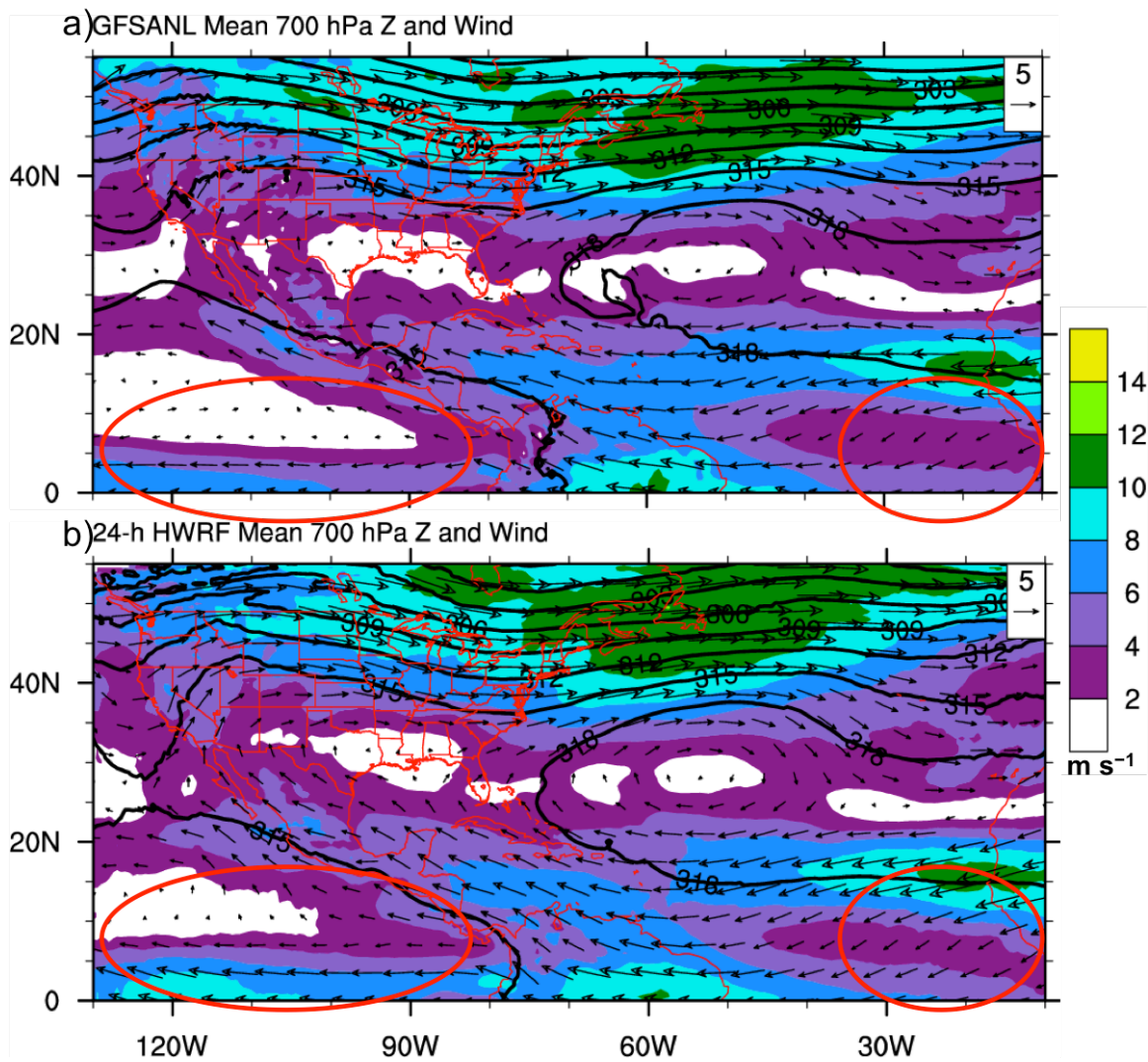


Figure 4.5: As in Fig. 4.3, except at 700 hPa.

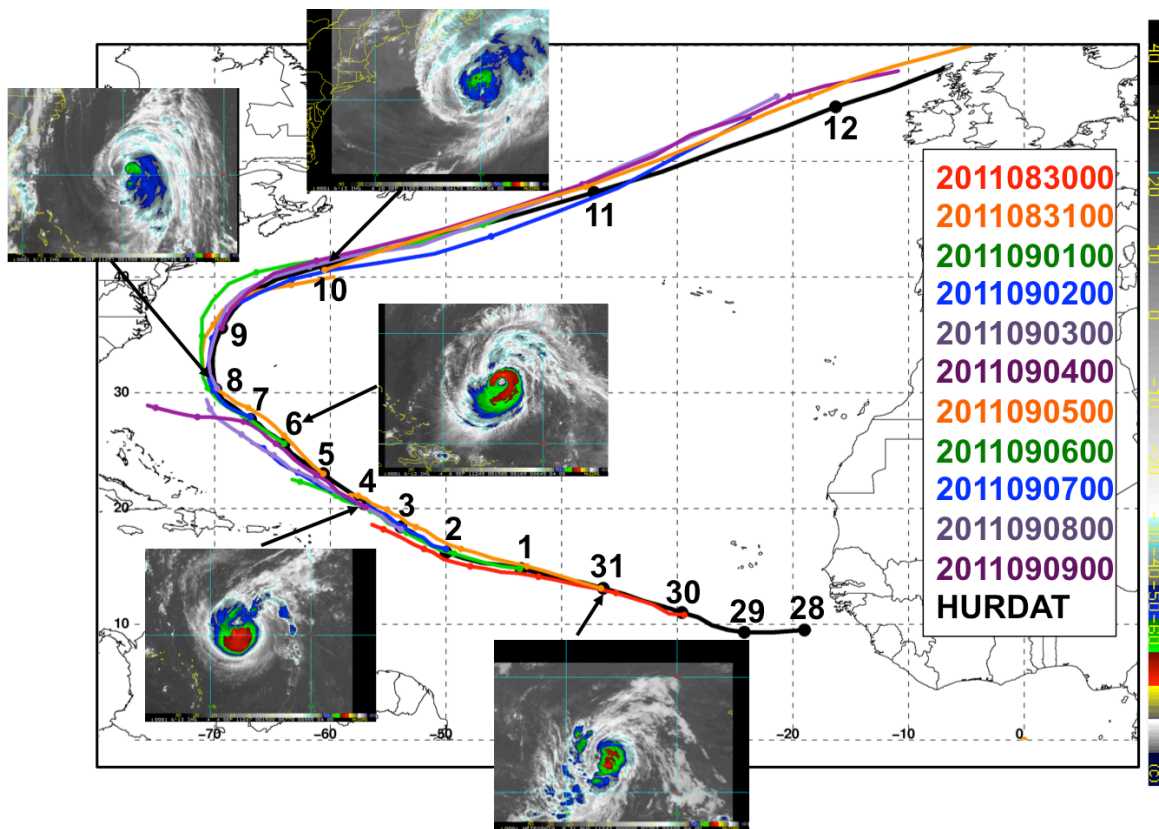


Figure 5.1: HURDAT (black line) and H213 track forecasts (color lines) of TC Katia (2011) for 0000 UTC 30 August–9 September. Enhanced infrared satellite imagery are shown as insets at select times. The satellite imagery was obtained from the RAMMB/CIRA archive.

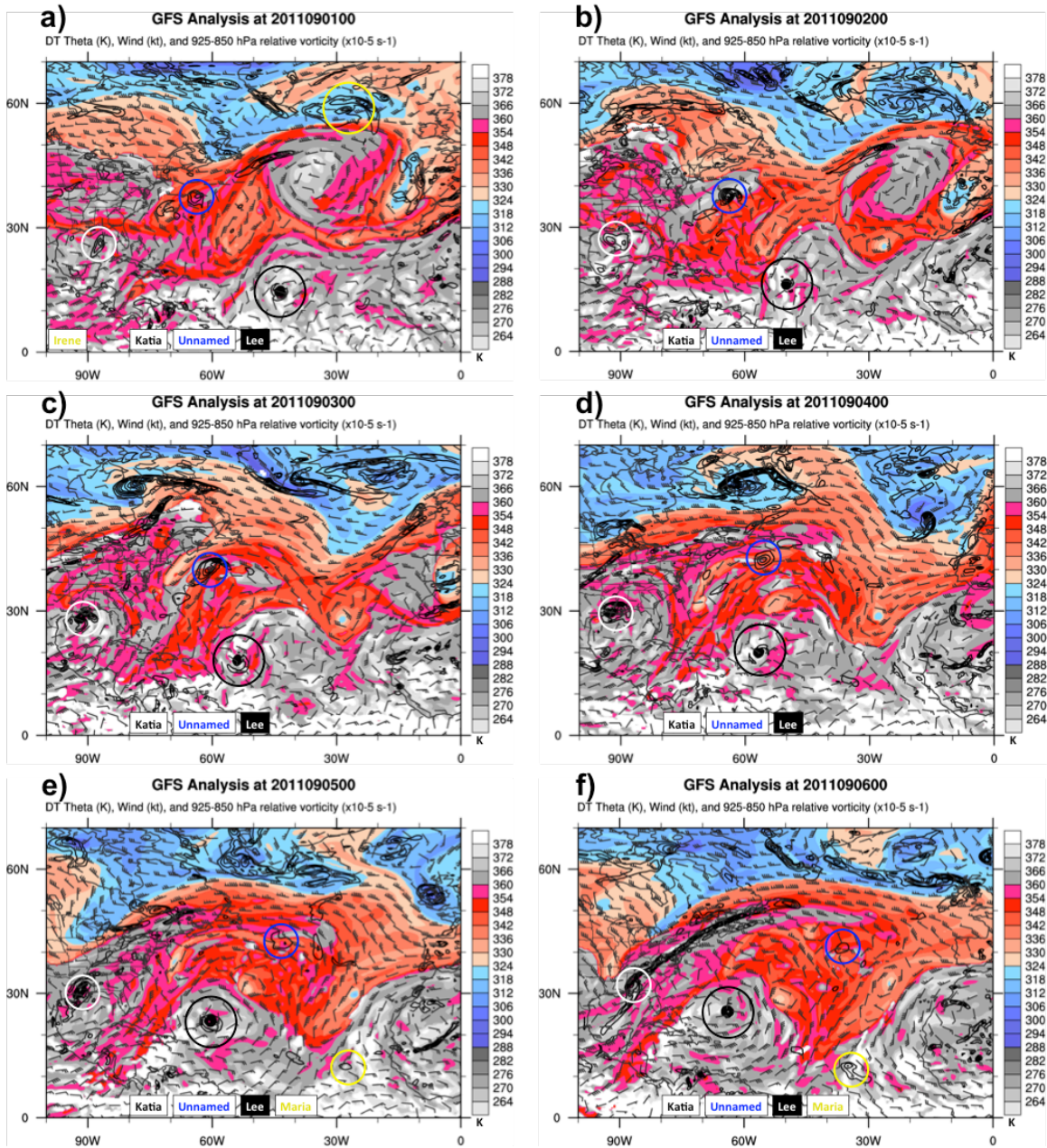


Figure 5.2: GFS analysis of DT potential temperature (shaded according to the color bar in K), wind (arrows in m/s), and 925–850 hPa layer mean relative vorticity (contours every  $2.0 \times 10^{-5} \text{ s}^{-1}$  starting at  $2.0 \times 10^{-5} \text{ s}^{-1}$ ) at 0000 YTC (a) 1, (b) 2, (c) 3, (d) 4, (e) 5, (f) 6, (g) 7, (h) 8, (i) 9, and (j) 10 September 2011. Locations of named TCs are identified by open circles according to the key at the bottom of each panel.

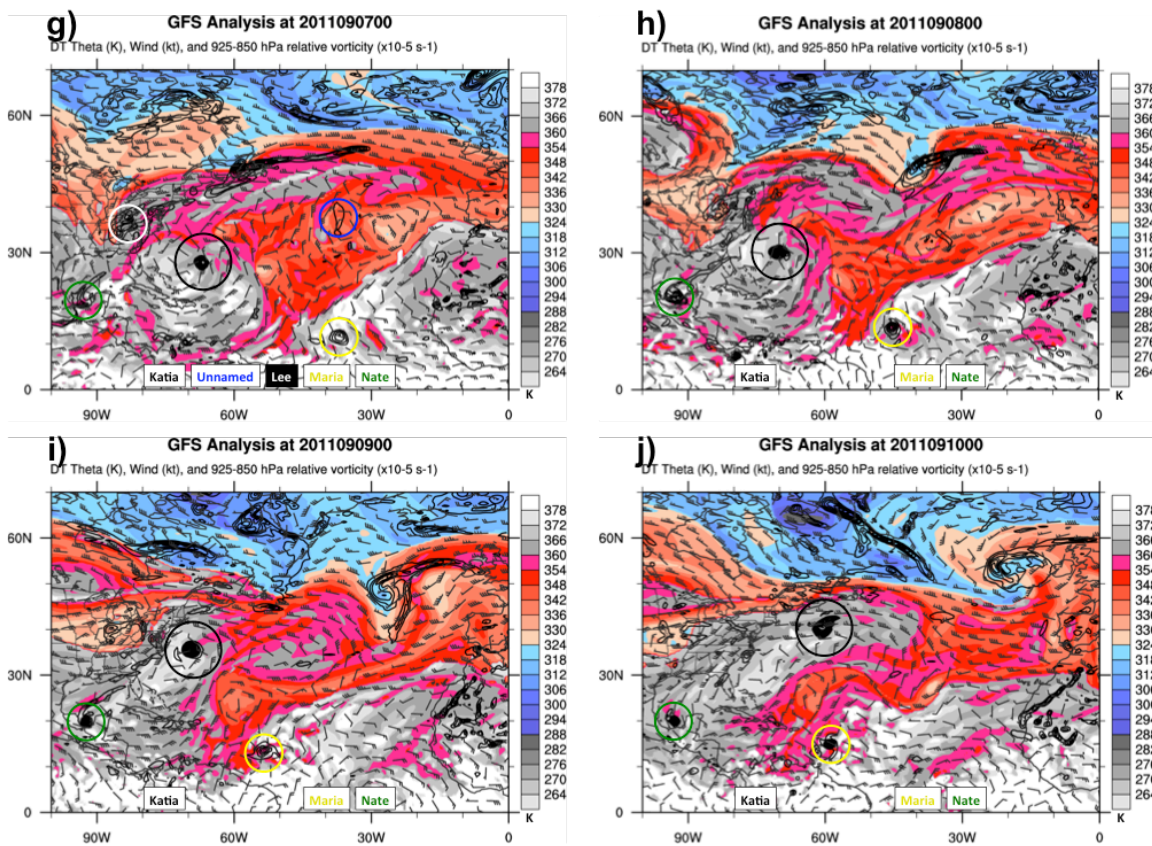


Figure 5.2 continued

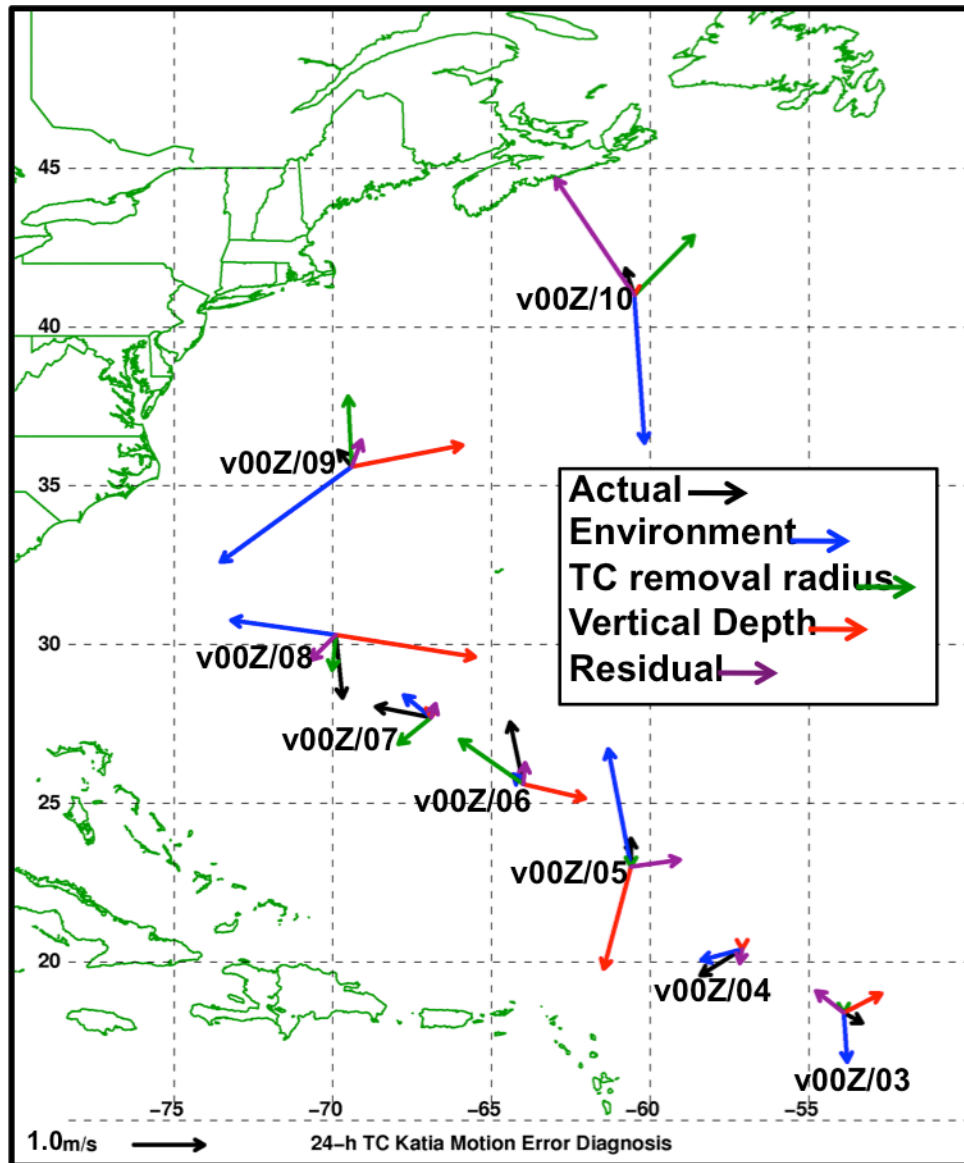


Figure 5.3: The TC motion error diagnostic equation terms ( $\text{m s}^{-1}$ ; reference vector plotted on lower left) for H213 24-h forecasts of TC Katia verifying at 0000 UTC 3–10 September 2011. The key on the right shows the arrow color for each term in the diagnostic equation.

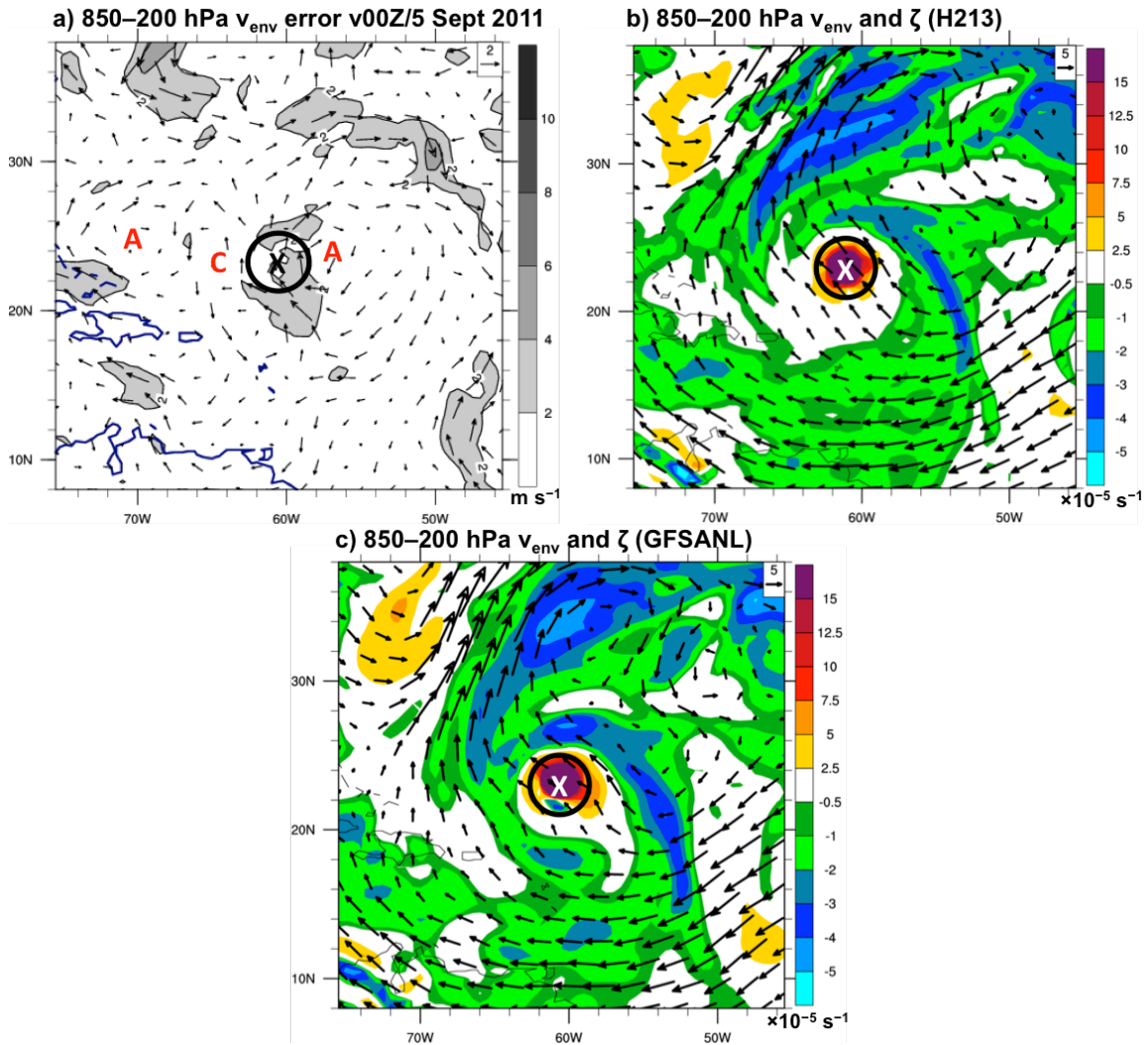


Figure 5.4: (a) H213 24-h forecast environment wind vector error (H213–GFSANL; arrows with magnitude shaded according to the grayscale in m/s), (b) H213 24-h forecast environment wind (arrows in m/s) and relative vorticity (shaded according to the color bar in  $\times 10^{-5} \text{ s}^{-1}$ ), and (c) GFS analysis environment wind (arrows in m/s) and relative vorticity (shaded according to the color bar in  $\times 10^{-5} \text{ s}^{-1}$ ) verifying at 0000 UTC 5 September 2011. The environment wind is defined here as the 850–200 hPa layer with a 2 degree TC removal radius. The TC position is marked ‘x’ and the TC removal radius by an open circle. Key cyclonic (marked ‘C’) and anticyclonic (marked ‘A’) circulation features in the wind error field are indicated in (a).

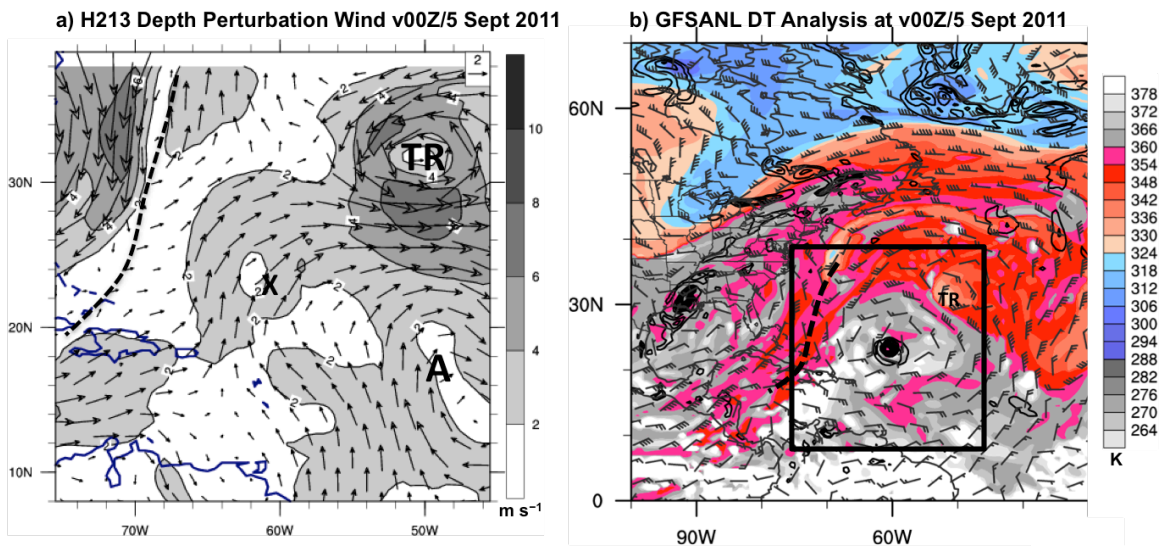


Figure 5.5: (a) H213 24-h forecast wind associated with the vertical depth error (arrows with magnitude shaded in m/s) and (b) DT analysis as in Fig. 5.2 verifying at 0000 UTC 5 September 2011. In (a), the TC position is marked 'x', midlatitude trough by a dashed line, anticyclonic circulation 'A', and cyclonic circulation 'TR'. The midlatitude trough and TR are also indicated in (b).

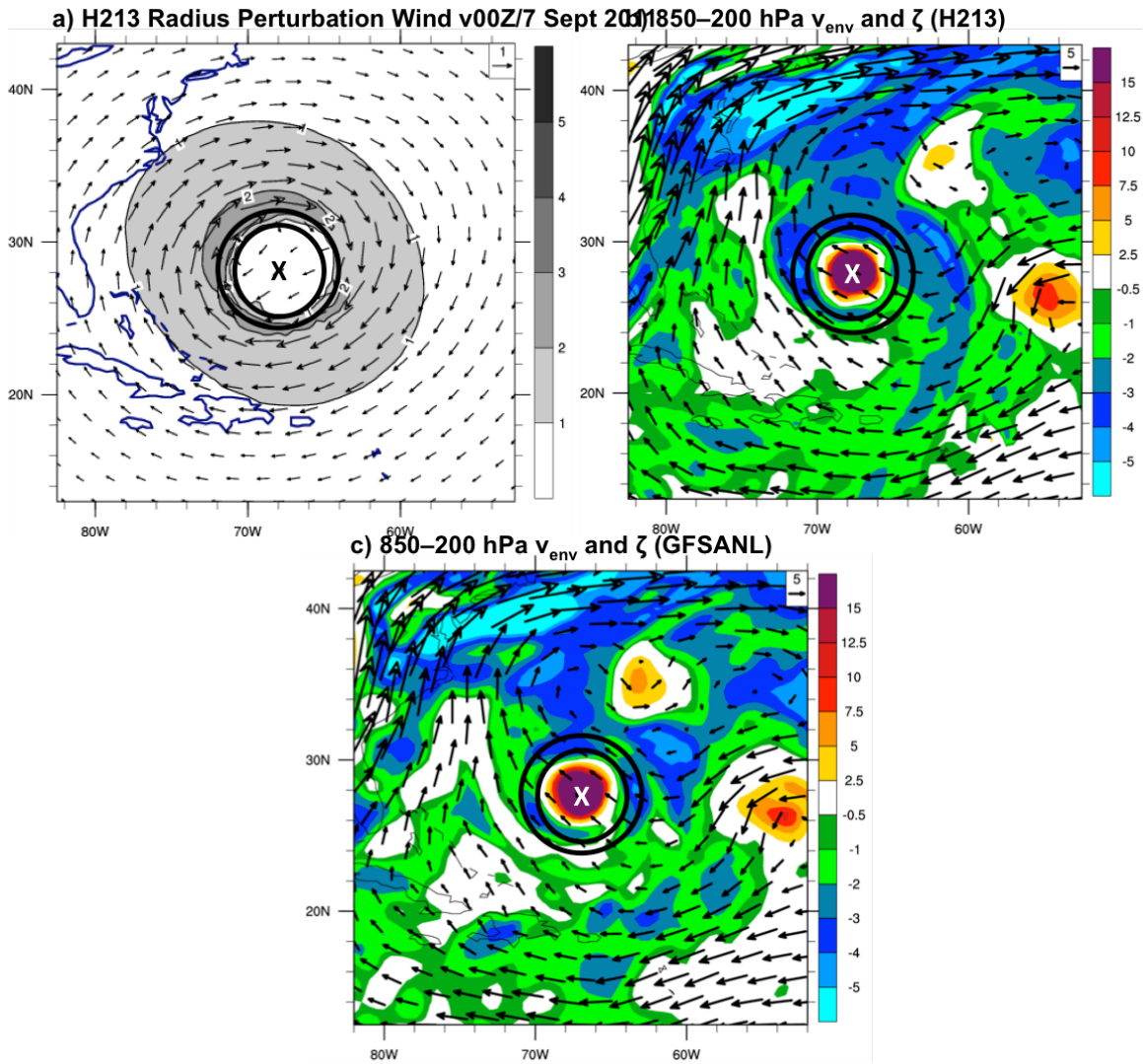


Figure 5.6: As in Fig. 5.4, except the verifying time is 0000 UTC 7 September 2011 and the wind error associated with the TC removal radius term is shown in (a).

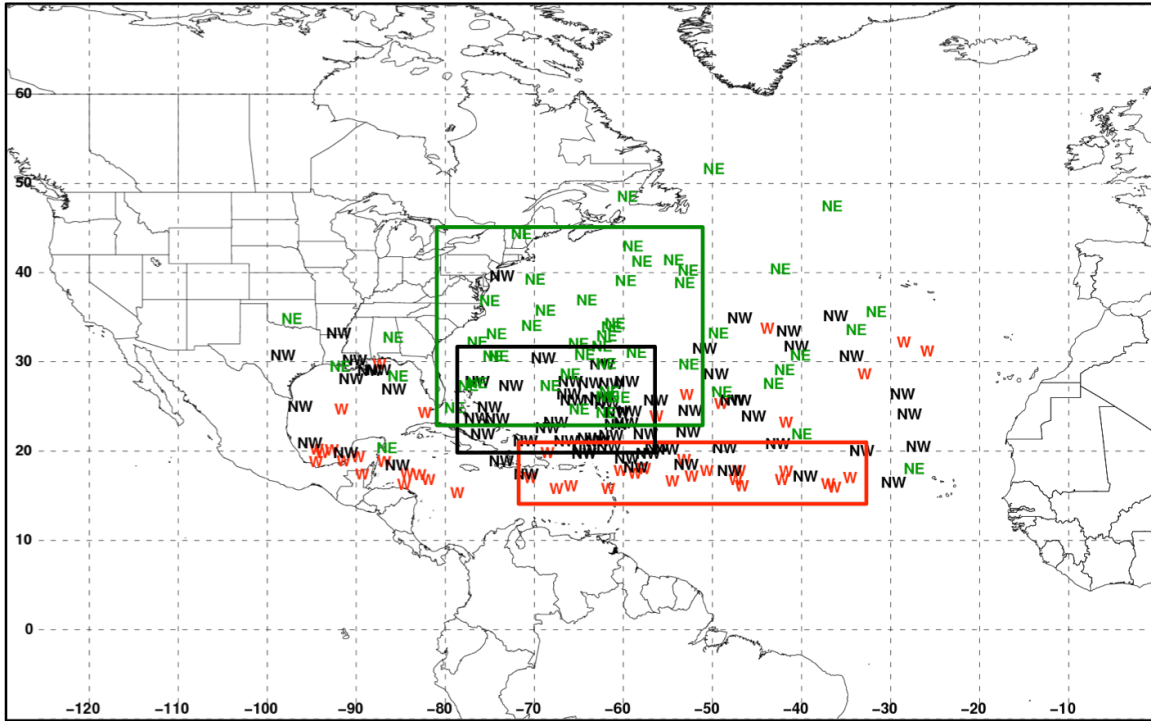


Figure 6.1: TC locations in the 24-h H213 forecasts stratified by TC motion as westward- (W; red), northwestward- (NW; black), and northeastward-moving (NE; green). The boxed regions encompass the TCs included in the time-mean maps shown in Figs. 6.5, 6.6, 6.8, 6.9, 6.11, and 6.12.

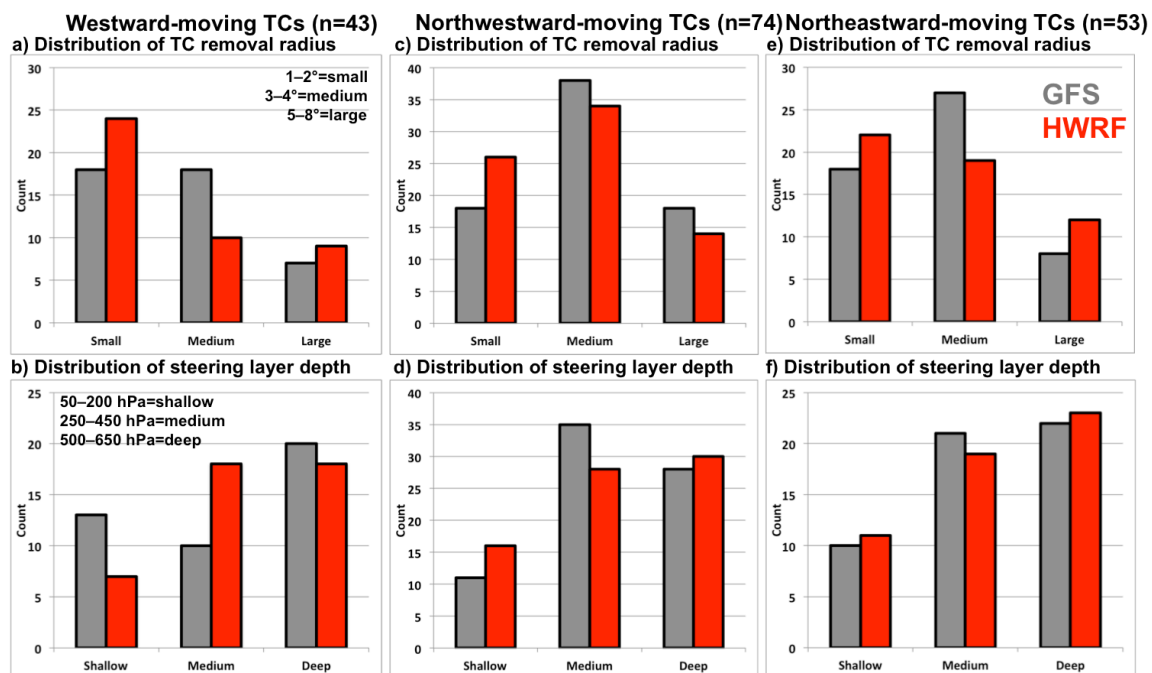
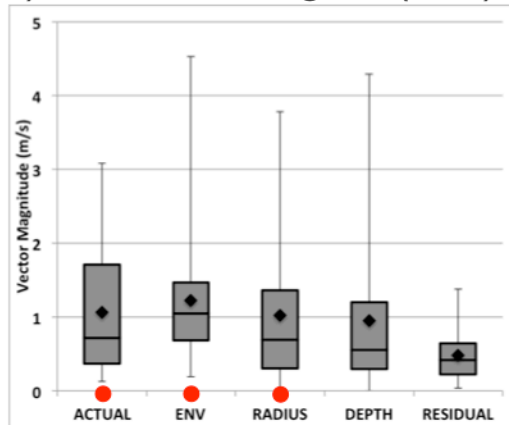
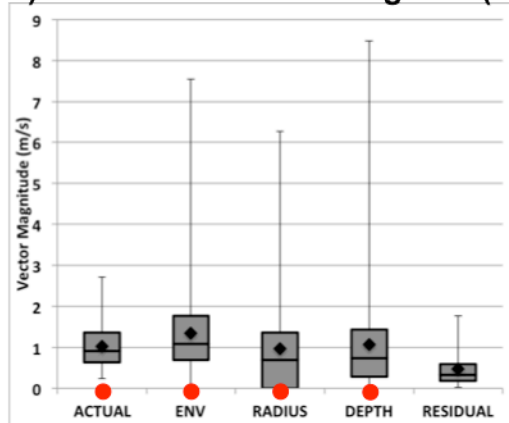


Figure 6.2: Histogram of (top) TC removal radius and (bottom) steering layer depth for 24-h H213 forecasts (red) and the verifying GFS analysis (gray) during the 2010–2012 TC seasons.

**a) Westward-moving TCs (n=43)**



**b) Northwestward-moving TCs (n=74)**



**c) Northeastward-moving TCs (n=53)**

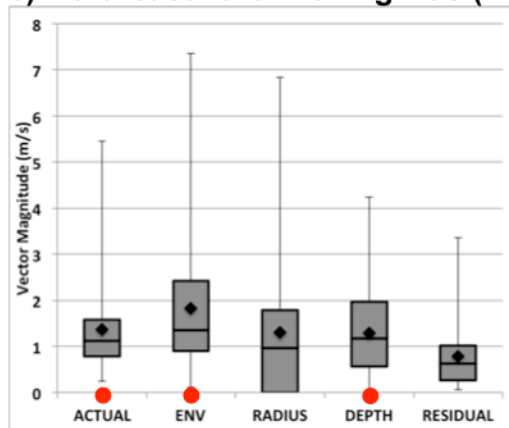


Figure 6.3: Box and whisker plots of the vector magnitude (m/s) of all the terms in the motion error diagnostic equation for (a) westward-moving, (b) northwestward-moving, and (c) northeastward-moving TCs during the H213 retrospective period. Terms that are significantly ( $\geq 95\%$ ) larger than the residual term are indicated by a filled red circle. The lower bound of the box marks the 25th percentile and the upper bound the 75th percentile, and the horizontal black line in the box marks the median value. The whiskers mark the maximum and minimum value, and the diamond marks the mean value.

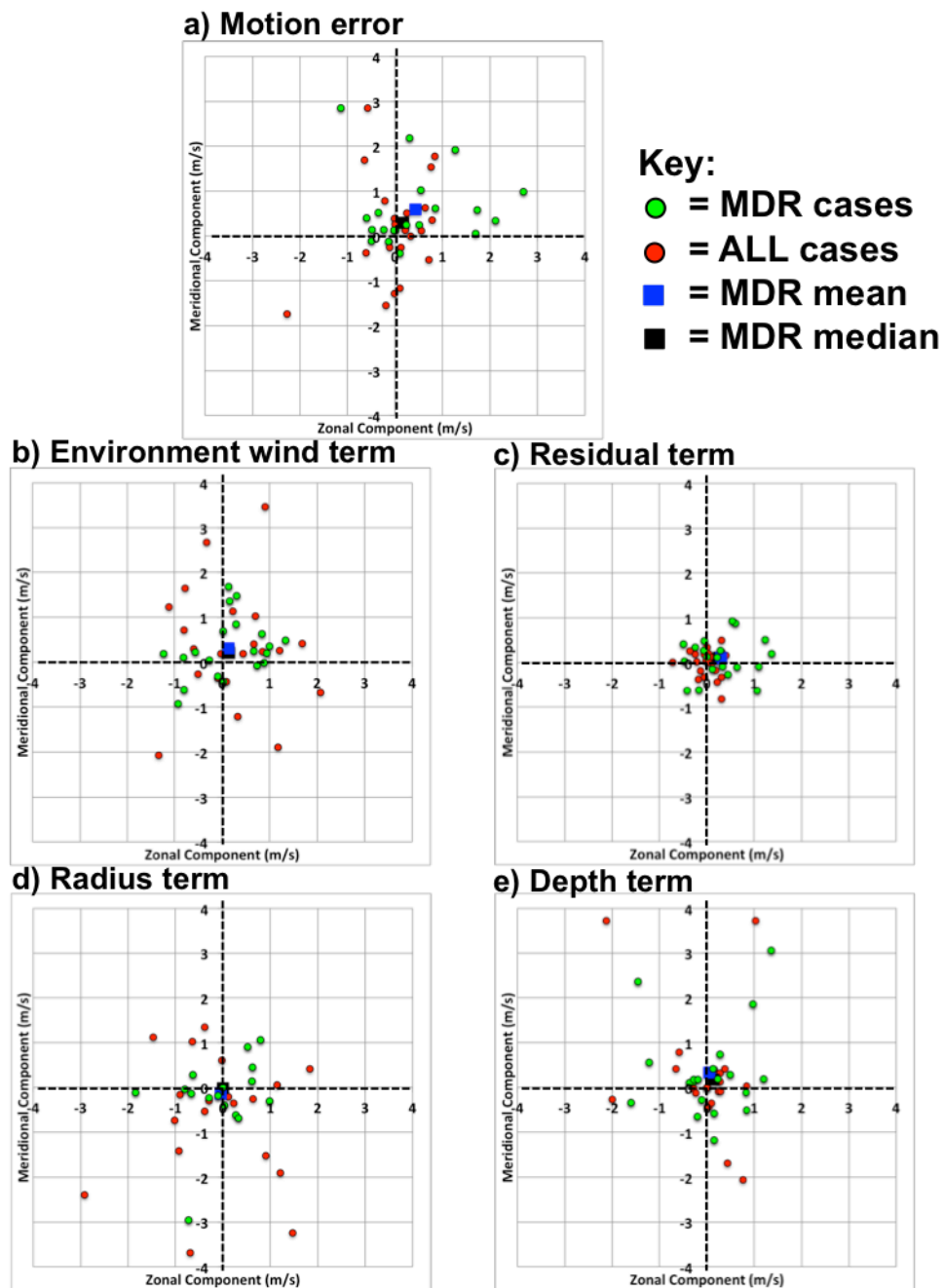


Figure 6.4: Scatterplot of the motion diagnostic terms for all westward-moving TCs during the H213 retrospective test. The green dots mark the TCs in the MDR region labeled on Fig. 6.1, and the red dots mark all other cases. The mean and median values are indicated by a blue and black square, respectively.

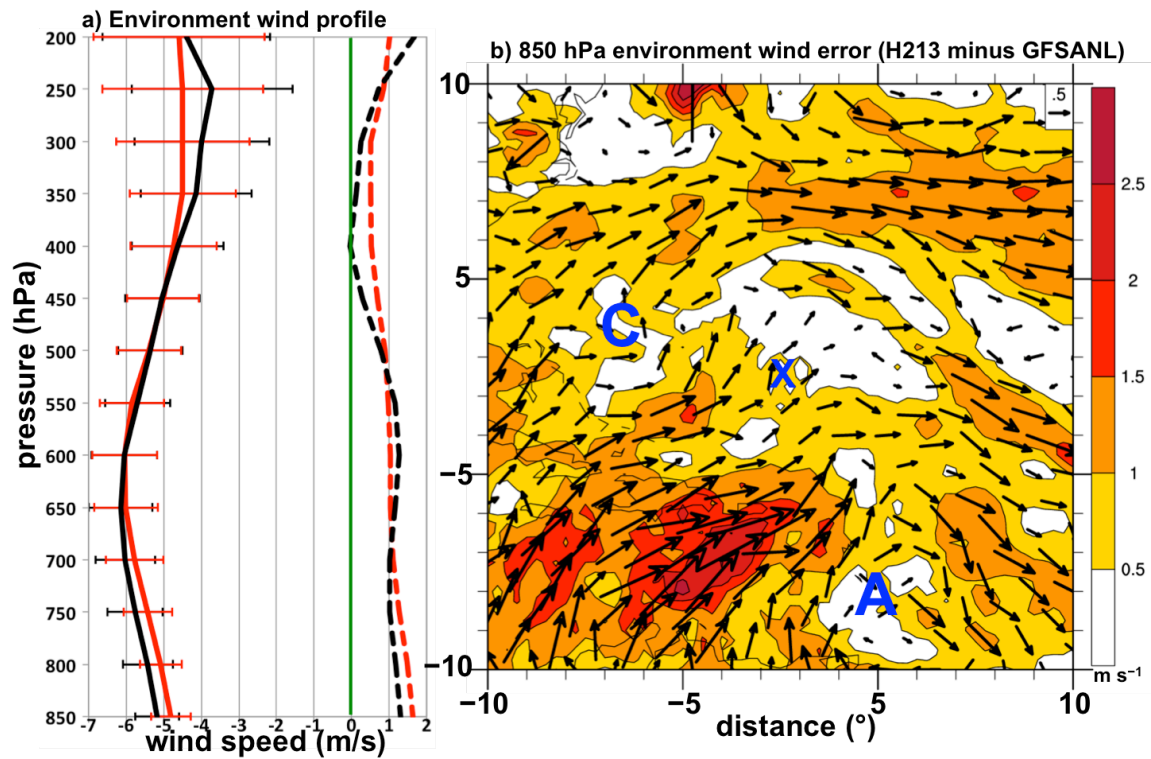


Figure 6.5: (a) Mean environment wind (m/s; zonal wind solid; meridional wind dashed) profile for 24-h H213 forecasts (red) and the corresponding GFS analysis (black). Error bars encompass the 90% confidence interval. (b) Mean 850 hPa environment wind error (H213–GFSANL; arrows with magnitude shaded according to the color bar in m/s) for the H213 retrospective period. Cyclonic (marked ‘C’) and anticyclonic (marked ‘A’) circulations and the composite TC location are indicated. The composite mean fields are in TC-relative coordinates.

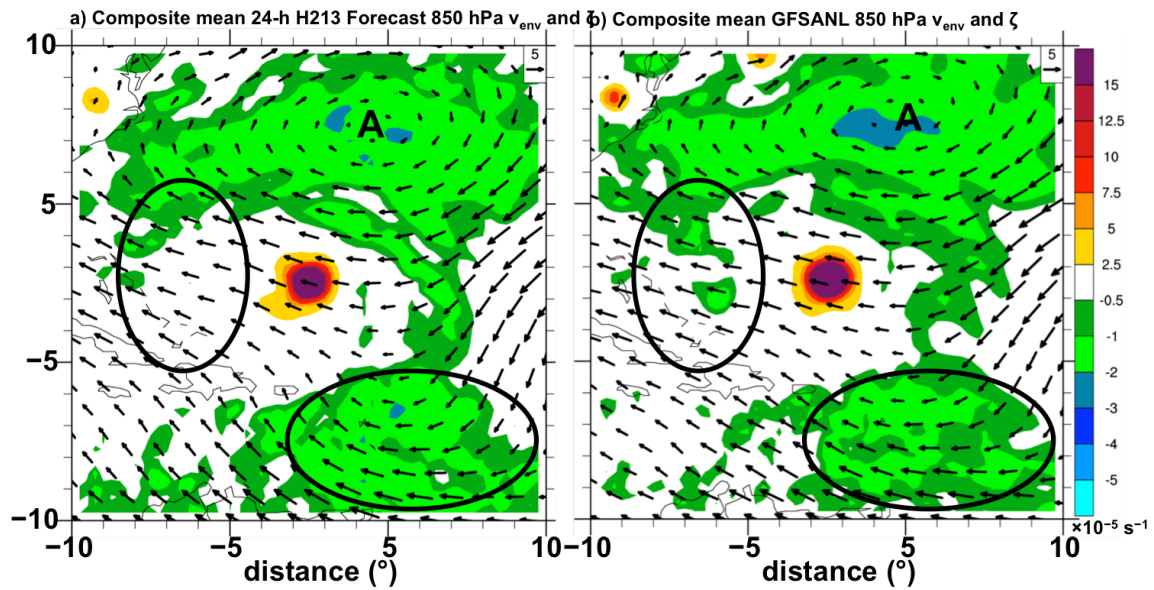


Figure 6.6: As in Fig. 6.5b, except showing 850 hPa environment wind (arrows in m/s) and relative vorticity (shaded according to the color bar in  $\times 10^{-5} \text{ s}^{-1}$ ) for (a) 24-h H213 forecasts and (b) GFS analyses.

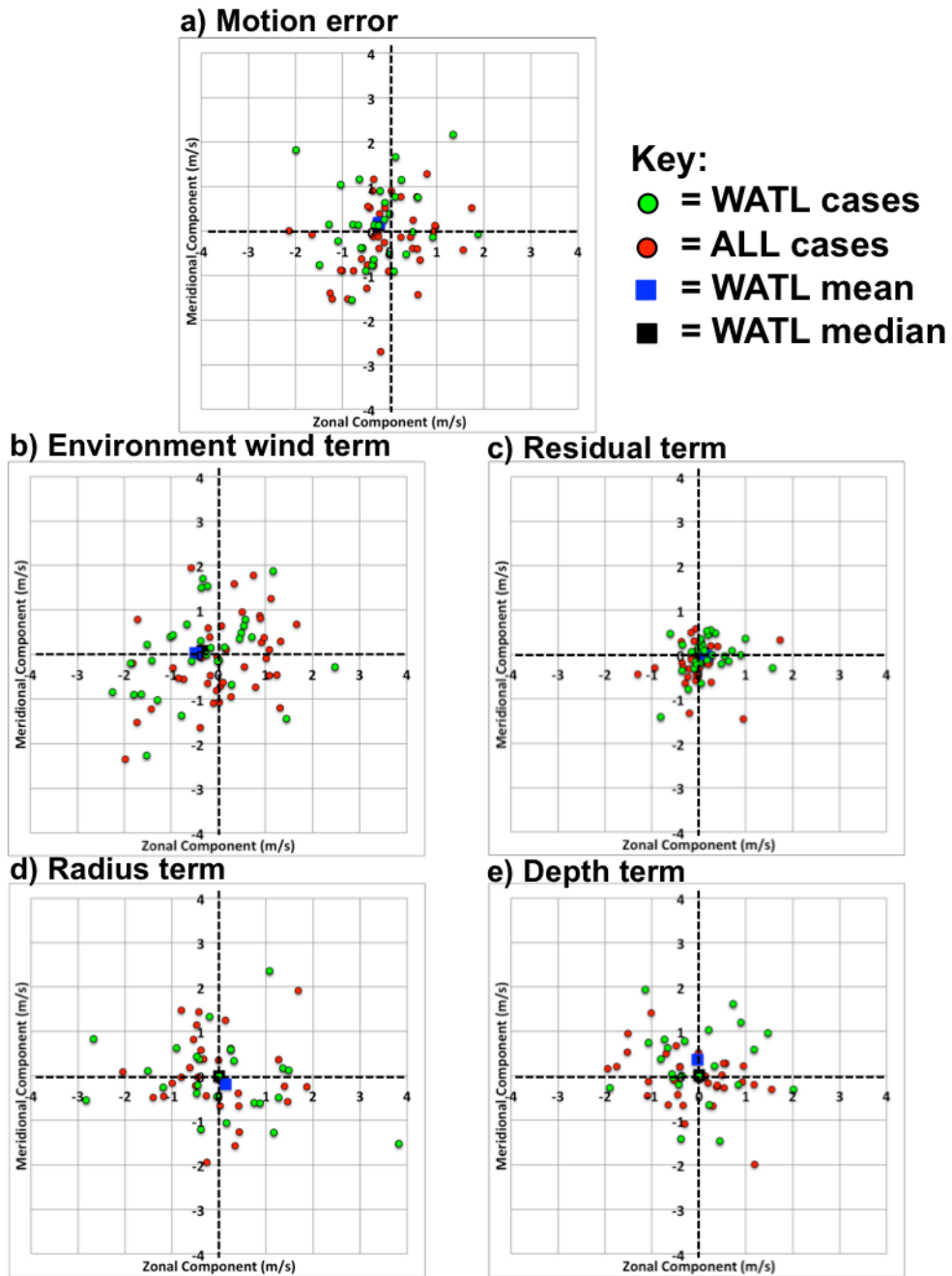


Figure 6.7: As in Fig. 6.4, except for northwestward-moving TCs.

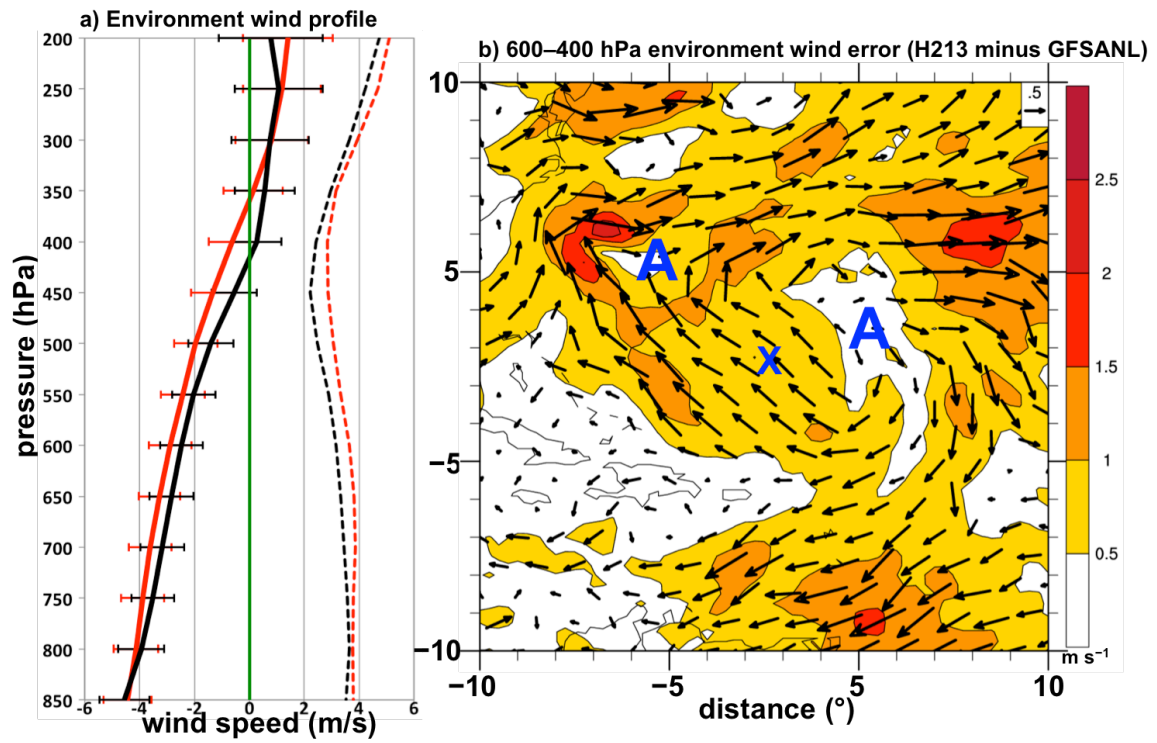


Figure 6.8: As in Fig. 6.5, except for northwestward-moving TCs (shown in Fig. 6.1). Also, the 600–400 hPa layer-mean is shown in (b).

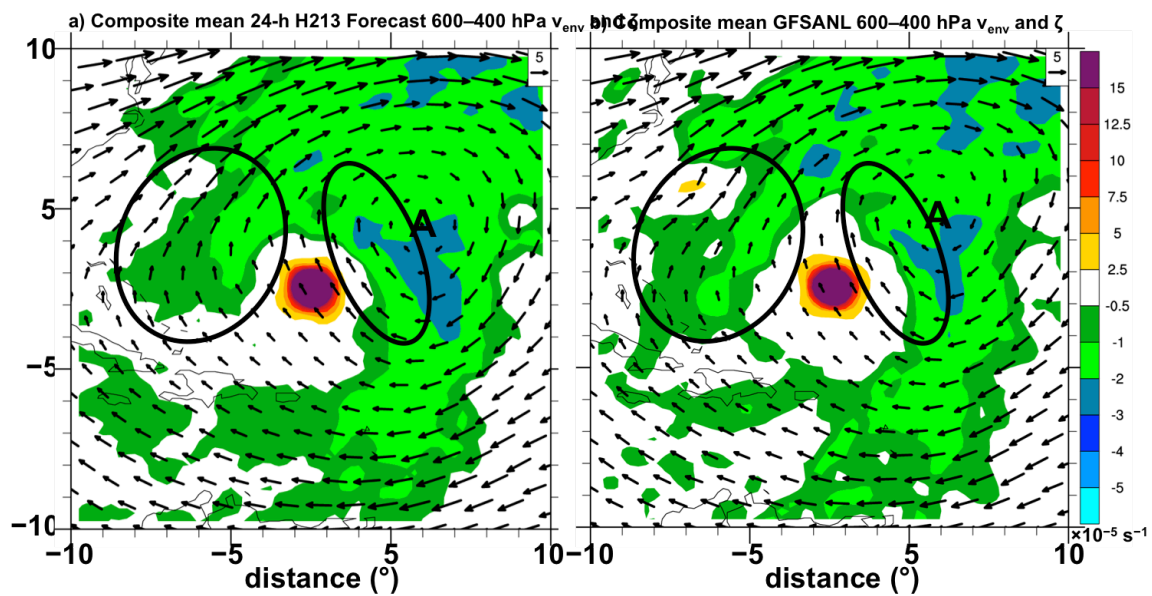


Figure 6.9: As in Fig. 6.6, except for northwestward-moving TCs and for the 600–400 hPa layer.

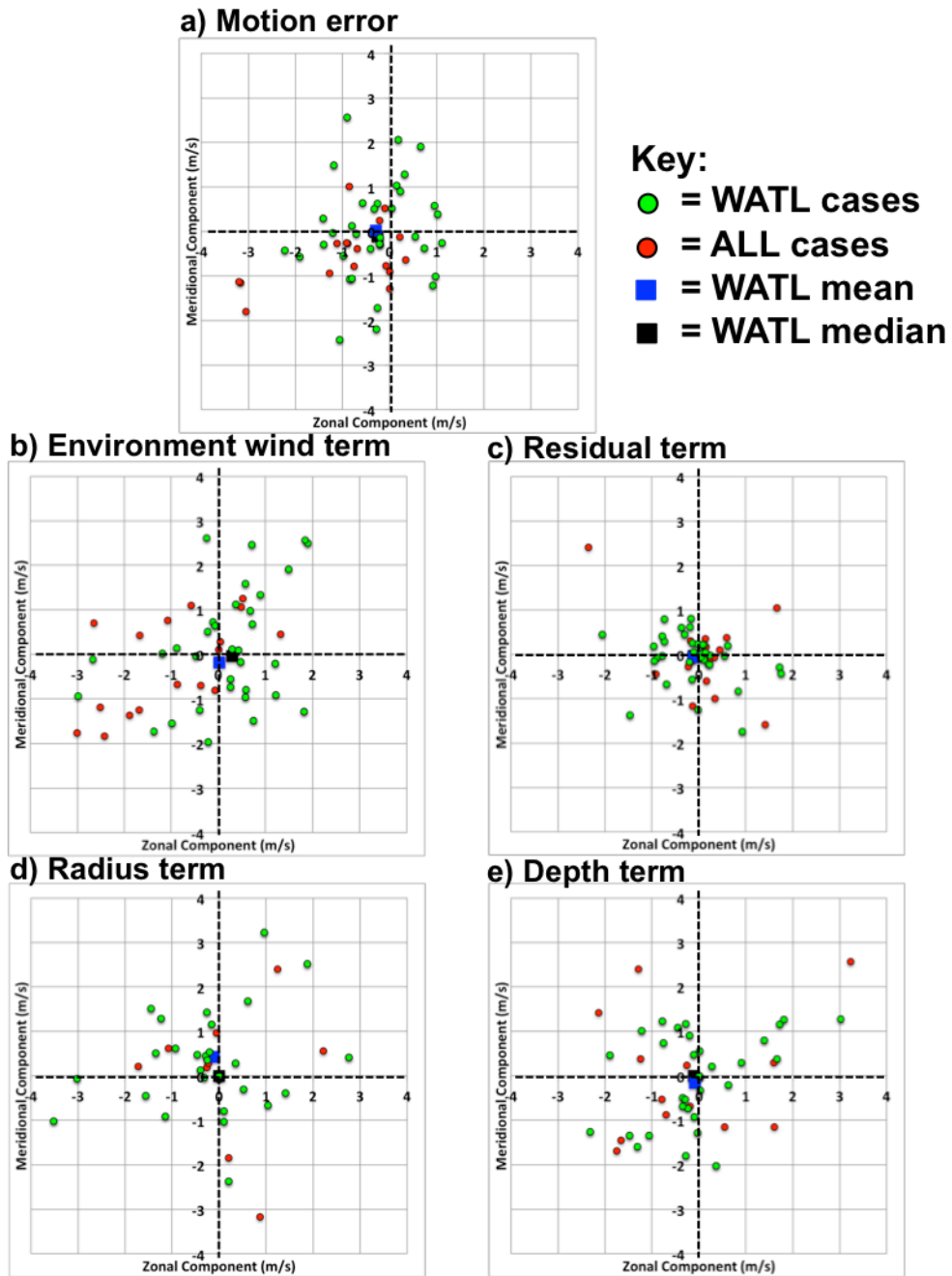


Figure 6.10: As in Fig. 6.4, except for northeastward-moving TCs.

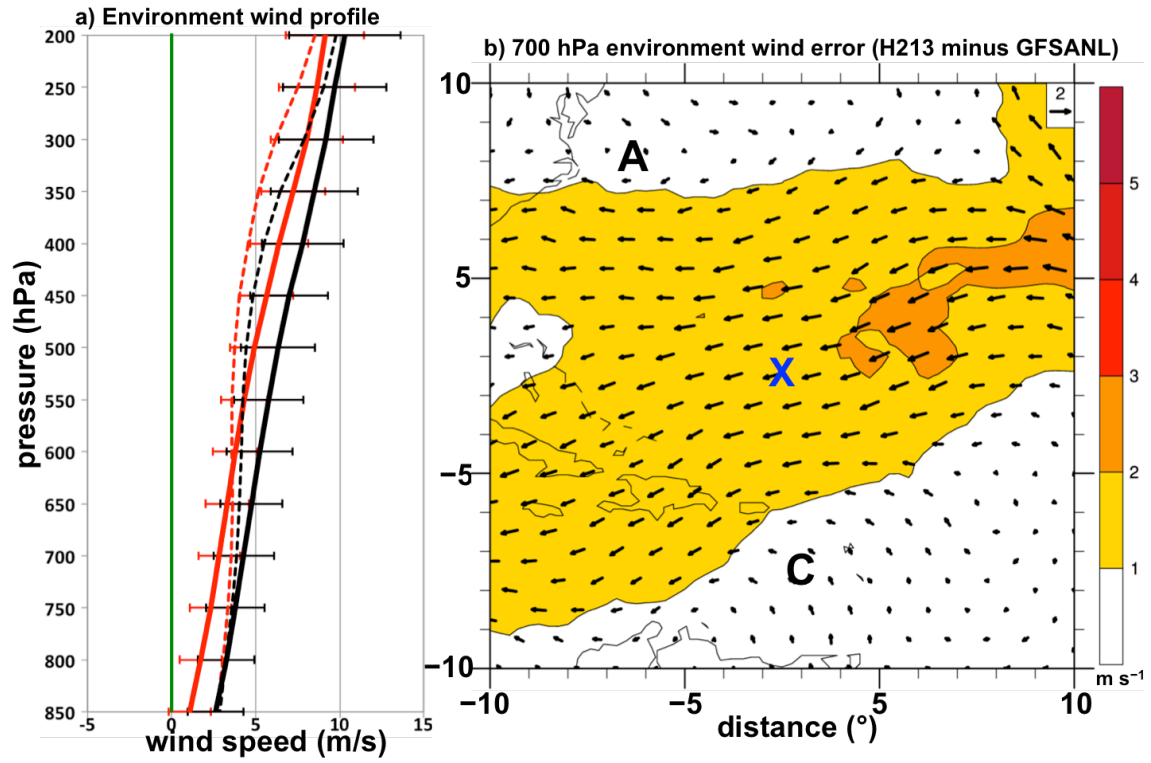


Figure 6.11: As in Fig. 6.5, except for northeastward-moving TCs (shown in Fig. 6.1). Also, the 700 hPa level is shown in (b).

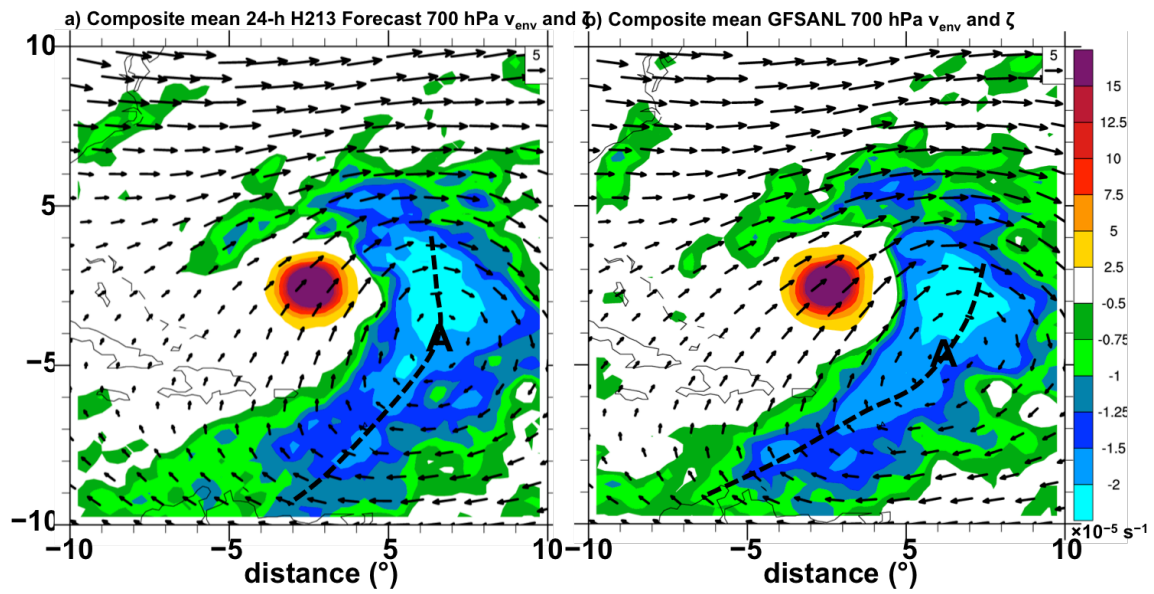


Figure 6.12: As in Fig. 6.6, except for northeastward-moving TCs and at the 700 hPa level.